

Analytical beam model revealing bone stresses in femur-implant compound structure

Lukas Pircher, Tilman A. Grünewald, Helga C. Lichtenegger & Christian Hellmich

To cite this article: Lukas Pircher, Tilman A. Grünewald, Helga C. Lichtenegger & Christian Hellmich (01 Dec 2024): Analytical beam model revealing bone stresses in femur-implant compound structure, Mechanics of Advanced Materials and Structures, DOI: [10.1080/15376494.2024.2419997](https://doi.org/10.1080/15376494.2024.2419997)

To link to this article: <https://doi.org/10.1080/15376494.2024.2419997>



© 2024 The Author(s). Published with license by Taylor & Francis Group, LLC



Published online: 01 Dec 2024.



Submit your article to this journal [↗](#)



View related articles [↗](#)



View Crossmark data [↗](#)

Analytical beam model revealing bone stresses in femur-implant compound structure

Lukas Pircher^a, Tilman A. Grünewald^b, Helga C. Lichtenegger^c, and Christian Hellmich^a

^aInstitute for Mechanics of Materials and Structures, TU Wien (Vienna University of Technology), Vienna, Austria; ^bAix-Marseille University, CNRS, Centrale Med, Institut Fresnel, Marseille, France; ^cInstitute of Physics and Materials Science, BOKU University, Vienna, Austria

ABSTRACT

We here introduce an analytical model for a preclinical femur-implant compound structure. This model extends standard Euler-Bernoulli-Saint-Venant theory by closed-form expressions for such shear stresses in thin-walled components, which arise from elastic material properties changing at the interfaces between bone and implant materials. Particularly noteworthy are stress singularities occurring at the generators of the cylindrical implants, which intersect the long axis of the bone shaft. This is fully consistent with observed major reorientations of bone fibrils following the implantation event, so that our novel mechanical model clearly indicates a case of micro-mechanobiology.

ARTICLE HISTORY

Received 18 October 2024
Accepted 18 October 2024

KEYWORDS

Analytical mechanics; composite beam theory; shear stress; local 3D equilibrium; magnesium implants; bone remodeling

1. Introduction

Pre-clinical studies are an indispensable element of biomedical research, and animal studies remain an indispensable part of preclinical research. However, as ethical concerns call for reduction of animal studies, the latter need to be very carefully designed [1], together with a maximized degree of evaluation and understanding of the outcome of corresponding investigations. In this context, mathematical modeling plays an ever increasing role [2], and the present contribution tackles the clearly needed improvement of corresponding mathematical models. More specifically, we focus on structural mechanics models for bone-implant structures occurring in standard animal models, more precisely on murine femoral shafts penetrated transcortically by magnesium implants [3, 4], see Figure 1. In this context, mathematical models have typically dealt with the degradation and corrosion process of the magnesium implants [6–8]—whereby Stefan problems, when cast into a rigorous mass conservation frame, play a central role [9, 10]. However, we here set a different focus, one on the mechanical behavior of the magnesium implant and the surrounding bone. This is motivated by a more recent discovery made possible through synchrotron small-angle scattering tomography [5]: significant changes in the bone microstructure evolve in the weeks and months after implantation; and this is so presumably because of a dramatically changed mechanical environment. In more detail, the implant causes the originally dominant orientation direction of fibrils along the long bone axis to shift toward a vortex-type (or “wrapping”) pattern around the

circumference of the implant [5]. Upon progressive implant resorption, however, the fibril orientation pattern transforms back toward the original configuration [5]. While noting that the 3D solid Finite Element Method (FEM) [11] is the current gold standard for mechanical organ-implant simulations [12], the current paper deals with a different approach, due to two main challenges faced by state-of-the-art finite element models constructed from microcomputed tomograms: (i) they do not allow for direct study of different design parameters such as implant shape or size, as any corresponding changes necessitate repeated, generally quite expensive numerical studies; and (ii) when tested on numerical convergence, large Finite element models of bony objects have been shown to actually fail [13], so that quantitatively relevant stress estimations obtained from the FEM are not assured, or rather, remain out of reach in many circumstances. In order to effectively tackle these open challenges, we here introduce an analytical bone-implant model, along the following lines: After geometrical representation of the femur-implant structure as two interpenetrating cylinders, one hollow and one filled, we recall the standard expressions for the normal stresses encountered in composite beams with cross-sections reflecting the aforementioned bone-implant compound structure. We continue Section 2 by re-calling the theory of shear stresses in thin-walled beams undergoing torsion and bending, before proposing corresponding extensions for composite beams of the aforementioned type, along with new expressions for shear stresses in such beams loaded by axial forces and bending moments. In

CONTACT Christian Hellmich  Christian.Hellmich@tuwien.ac.at  Institute for Mechanics of Materials and Structures, TU Wien (Vienna University of Technology), Vienna, Austria.

© 2024 The Author(s). Published with license by Taylor & Francis Group, LLC

This is an Open Access article distributed under the terms of the Creative Commons Attribution License (<http://creativecommons.org/licenses/by/4.0/>), which permits unrestricted use, distribution, and reproduction in any medium, provided the original work is properly cited. The terms on which this article has been published allow the posting of the Accepted Manuscript in a repository by the author(s) or with their consent.

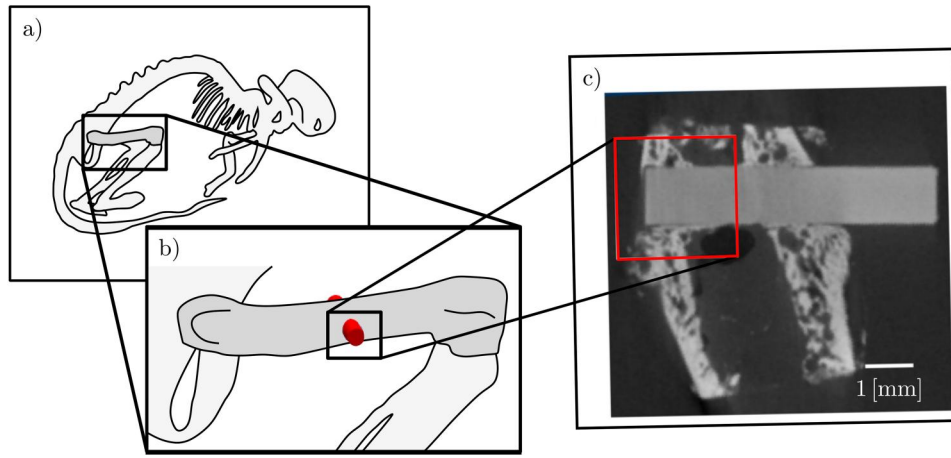


Figure 1. Preclinical trial of magnesium implants in murine femora: (a) skeleton of rat with right hindlimp; (b) position of magnesium pin in right femoral shaft, (c) microCT slice depicting implant one month after implantation, image reproduced from [5], under license CC by 4.0.

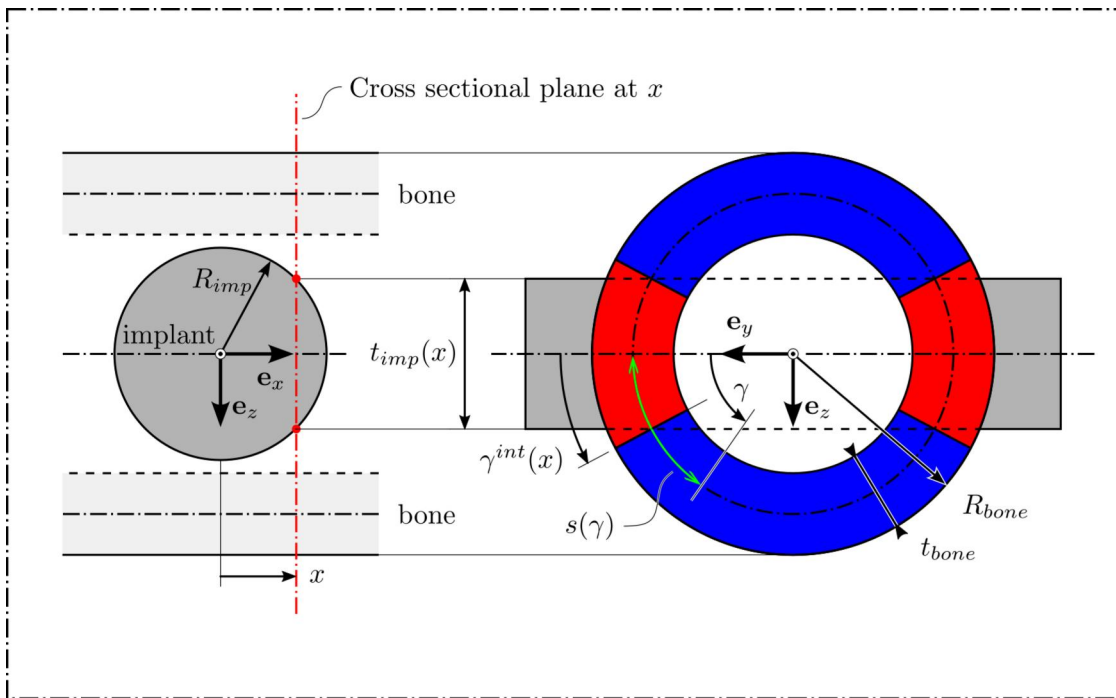


Figure 2. Definition of system geometry, by means of bone radius R_{bone} , bone thickness t_{bone} , and implant radius R_{imp} ; implant thickness t_{imp} and interface-related polar angle γ_{int} depend on axial distance x from the implant axis; positions on the bone profile curve are given in terms of the polar angle γ and the arc length s .

Section 3, these expressions are then evaluated for practically relevant geometrical and material properties, and illustrated in terms of corresponding stress distributions. Finally, **Section 4** contains a discussion in view of tomograms elucidating microstructural changes in bone tissue in the vicinity of the implant, followed by the limitations of the present approach and corresponding potential future activities.

2. Mathematical formulation

2.1. Geometrical system, elastic properties, as well as mechanical forces and stresses

We consider two penetrating cylinders, one hollow and one filled, with the first representing a cortical bone shaft and the second representing an implant, see **Figures 2** and **3**.

The axes of these cylinders intersect, while lying perpendicular to each other. This geometrical system is defined through the outer radius of the hollow cylinder, R_{bone} , by the thickness of this cylindrical shell, t_{bone} , and by the radius of the filled implant cylinder, R_{imp} , see **Figure 2** and **Table 1**.

The axis of the first cylinder is regarded as beam axis with orientation \mathbf{e}_x , and the corresponding composite beam, which consists of two materials, cortical bone and magnesium with elastic properties according to **Table 1**, is subjected to second-order tensorial Cauchy stress states $\boldsymbol{\sigma}$ of the form [15].

$$\boldsymbol{\sigma} = \sigma_{xx} \mathbf{e}_x \otimes \mathbf{e}_x + \sigma_{xy} (\mathbf{e}_x \otimes \mathbf{e}_y + \mathbf{e}_y \otimes \mathbf{e}_x) + \sigma_{xz} (\mathbf{e}_x \otimes \mathbf{e}_z + \mathbf{e}_z \otimes \mathbf{e}_x) \quad (1)$$

with σ_{xx} , σ_{xy} , and σ_{xz} as the non-vanishing components of the stress tensor; and with \mathbf{e}_x , \mathbf{e}_y , and \mathbf{e}_z as the unit vectors forming

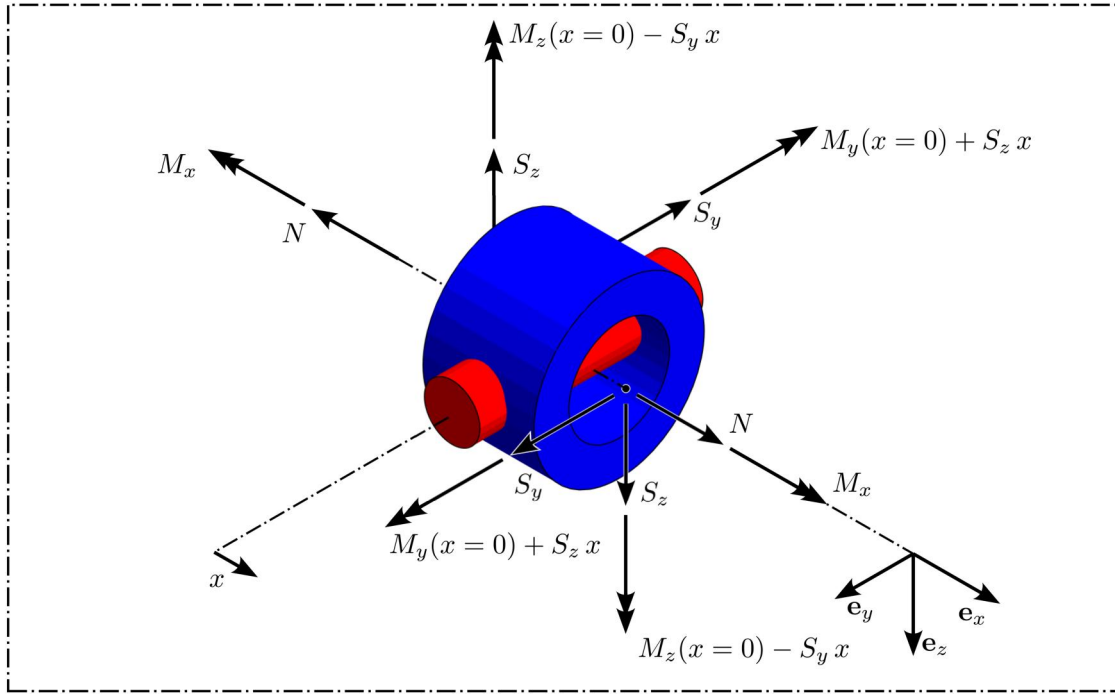


Figure 3. Resultant forces acting on bone-implant compound structure (femoral shaft portion in blue, with axis direction \mathbf{e}_x ; magnesium implant in red, with axis direction \mathbf{e}_y); quantified in terms of beam theory-related internal force quantities N (axial force), M_y and M_z (bending moments), S_y and S_z (shear forces), and M_x (torsional moment).

Table 1. Geometrical and mechanical properties encountered in preclinical study [5].

Quantity	Value	Source
(Axial) elastic modulus of cortical bone, E_{bone}	25 GPa	[13]
(Isotropic) elastic modulus of magnesium, E_{imp}	37 GPa	[14]
Radius of femoral shaft, R_{bone}	2.45 mm	[5]
Thickness of cortical shell, t_{bone}	1.0 mm	[5]
Radius of implant cylinder, R_{imp}	0.8 mm	[5]

the orthonormal basis depicted in Figure 3. These stress states are associated with internal forces, namely axial forces N , shear forces S_y and S_z , torsional moments M_x , as well as bending moments M_y and M_z . Such internal forces can be obtained from ground reaction forces [16] in combination with an inverse dynamics model for the overall musculoskeletal system [17]. The latter reference provides, at the center of the femoral shaft of a rat, the temporal evolution of the aforementioned internal forces over a single trotting stride. Temporal averaging over this stride yields the following values,

$$\begin{aligned}
 N &= -8.03 \text{ N} & S_y &= -1.15 \text{ N} \\
 S_z &= -0.16 \text{ N} & M_x &= -1.15 \text{ Nmm} \\
 M_y(x=0) &= 12.78 \text{ Nmm} & M_z(x=0) &= -1.20 \text{ Nmm}
 \end{aligned} \quad (2)$$

While the forces and the torsional moments will be considered as constant along the beam axis in the vicinity of implant, the standard equilibrium conditions for slender beams undergoing bending, see e.g. [15, 18] and Appendix,

$$\frac{dM_y}{dx} = S_z \quad \frac{dM_z}{dx} = -S_y \quad (3)$$

entail correspondingly linear trends of the bending moments,

$$M_y(x) = M_y(x=0) + S_z x \quad M_z(x) = M_z(x=0) - S_y x \quad (4)$$

2.2. Normal stresses according to composite beam theory

Following the standard composite beam theory [18–20], where the axial normal strains ε_{xx} are linearly distributed throughout the cross sections of the composite beam, the normal stress distributions over the cross sections of the investigated bone-implant structure are linked to the axial force N and the bending moments M_y and M_z through the relation

$$\sigma_{xx}^N = \frac{E(x, s)}{E_{bone}} \frac{N}{A_{bone}(x) + \frac{E_{imp}}{E_{bone}} A_{imp}(x)} \quad (5)$$

$$\sigma_{xx}^{M_y} = \frac{E(x, s)}{E_{bone}} \frac{M_y(x)z(s)}{I_{y, bone}(x) + \frac{E_{imp}}{E_{bone}} I_{y, imp}(x)} \quad (6)$$

$$\sigma_{xx}^{M_z} = -\frac{E(x, s)}{E_{bone}} \frac{M_z(x)y(s)}{I_{z, bone}(x) + \frac{E_{imp}}{E_{bone}} I_{z, imp}(x)} \quad (7)$$

In Eqs. (5)–(7), s denotes the arc length labeling positions on the midsurface of the bone shell and its extensions into the implant. It reads mathematically as

$$s(\gamma) = \gamma \left(R_{bone} - \frac{t_{bone}}{2} \right) \leftrightarrow \gamma(s) = \frac{s}{\left(R_{bone} - \frac{t_{bone}}{2} \right)} \quad (8)$$

with the polar angle γ as depicted in Figure 2. The arc length is related to the Cartesian coordinates y and z through

$$\begin{aligned}
 y(s) &= \cos[\gamma(s)] \times \left(R_{bone} - \frac{t_{bone}}{2} \right) \\
 &= \cos \left[\frac{s}{\left(R_{bone} - \frac{t_{bone}}{2} \right)} \right] \times \left(R_{bone} - \frac{t_{bone}}{2} \right) \quad (9)
 \end{aligned}$$

and

$$\begin{aligned} z(s) &= \sin[\gamma(s)] \times \left(R_{bone} - \frac{t_{bone}}{2} \right) \\ &= \sin \left[\frac{s}{\left(R_{bone} - \frac{t_{bone}}{2} \right)} \right] \times \left(R_{bone} - \frac{t_{bone}}{2} \right) \end{aligned} \quad (10)$$

Furthermore, in Eqs. (5)–(7), A_{bone} denotes the cross-sectional area of bone; A_{imp} denotes the area of implant replacing former bone; $I_{y,bone}$ and $I_{z,bone}$, respectively, are the second-order area moments around the y -axis and the z -axis of the bone portion within a cross-section through the bone-implant compound; and $I_{y,imp}$ and $I_{z,imp}$, respectively, are the second-order area moments around the y -axis and the z -axis of the implant portion within a cross-section through the bone-implant compound. We explicitly note that the geometrical properties of the cross-sections, such as areas and area moments, explicitly depend on the coordinate of the beam axis, x . In this context, the cross-sectional areas and area moments are quantified in terms of the cross-section-specific polar angle of the bone-implant interface, which we denote as γ_{int} . It can be given in terms of the section-specific implant thickness t_{imp} and the outer radius of the femoral shaft, R_{bone} , through

$$\gamma_{int}(x) = \arcsin \left(\frac{\frac{t_{imp}(x)}{2}}{R_{bone} - \frac{t_{bone}}{2}} \right) \quad (11)$$

The thickness t_{imp} of the cross-sectional portion made up by the implant can, in turn, be expressed through the axial distance from the cylindrical axes intersection point, denoted as x , and the implant radius, *via*

$$t_{imp}(x) = 2\sqrt{(R_{imp})^2 - x^2} \quad (12)$$

see Figure 2. The cross sectional properties of the hollow bone cylinder without implant, occurring at $x \leq R_{imp}$ and $x \geq R_{imp}$, read as

$$A_{bone} = 2\pi \left[R_{bone} - \frac{t_{bone}}{2} \right] t_{bone} \quad (13)$$

$$I_{y,bone} = \frac{1}{4}\pi \left[(R_{bone})^4 - (R_{bone} - t_{bone})^4 \right] \quad (14)$$

$$I_{z,bone} = \frac{1}{4}\pi \left[(R_{bone})^4 - (R_{bone} - t_{bone})^4 \right] \quad (15)$$

$$A_{imp} = I_{y,imp} = I_{z,imp} = 0 \quad (16)$$

The cross sectional properties of cross sections comprising both bone and implant, occurring at $-R_{imp} < x < R_{imp}$, read as

$$A_{bone}(x) = (2\pi - 4\gamma_{int}(x)) \left[R_{bone} - \frac{t_{bone}}{2} \right] t_{bone} \quad (17)$$

$$\begin{aligned} I_{y,bone}(x) &= \frac{1}{4}(\pi - 2\gamma_{int}(x) + \sin[2\gamma_{int}(x)]) \times \\ &\times \left[(R_{bone})^4 - (R_{bone} - t_{bone})^4 \right] \end{aligned} \quad (18)$$

$$\begin{aligned} I_{z,bone}(x) &= \frac{1}{4}(\pi - 2\gamma_{int}(x) - 2\cos[\gamma_{int}(x)] \sin[\gamma_{int}(x)]) \times \\ &\times \left[(R_{bone})^4 - (R_{bone} - t_{bone})^4 \right] \end{aligned} \quad (19)$$

$$A_{imp}(x) = 4\gamma_{int}(x) \left[R_{bone} - \frac{t_{bone}}{2} \right] t_{bone} \quad (20)$$

$$\begin{aligned} I_{y,imp}(x) &= \frac{1}{2}(\gamma_{int}(x) - \cos[\gamma_{int}(x)] \sin[\gamma_{int}(x)]) \times \\ &\times \left[(R_{bone})^4 - (R_{bone} - t_{bone})^4 \right] \end{aligned} \quad (21)$$

$$\begin{aligned} I_{z,imp}(x) &= \frac{1}{2}(\gamma_{int}(x) + \cos[\gamma_{int}(x)] \sin[\gamma_{int}(x)]) \times \\ &\times \left[(R_{bone})^4 - (R_{bone} - t_{bone})^4 \right] \end{aligned} \quad (22)$$

The cross-sectional compartments hosting bone- and implant-related axial Young's modulus values, E_{bone} and E_{imp} , are characterized through of the following function of axial position x and arc length s

$$\begin{aligned} E(x, s) &= E_{imp} - (E_{imp} - E_{bone}) \times \\ &\left\{ \begin{aligned} &H \left[s - \gamma_{int}(x) \times \left(R_{bone} - \frac{t_{bone}}{2} \right) \right] \\ &- H \left[s - [\pi - \gamma_{int}(x)] \times \left(R_{bone} - \frac{t_{bone}}{2} \right) \right] \\ &+ H \left[s - [\pi + \gamma_{int}(x)] \times \left(R_{bone} - \frac{t_{bone}}{2} \right) \right] \\ &- H \left[s - [2\pi - \gamma_{int}(x)] \times \left(R_{bone} - \frac{t_{bone}}{2} \right) \right] \end{aligned} \right\} \end{aligned} \quad (23)$$

with H denoting the Heaviside step function; $H(\xi < 0) = 0$ and $H(\xi > 0) = 1$. This function allows for an elegant representation of the jump encountered in the elastic modulus when moving from the bone to the implant portion of the considered compound structure.

2.3. Axial gradients of normal stresses occurring in local 3D equilibrium conditions

2.3.1. Motivation

As a starting point, we follow the classical beam theory approaches [15, 18] where gradients in axial forces arise from shear tractions on the beam surfaces (for the present application, the latter may be realized in terms of point loads associated with muscle attachments), and where shear stresses are due to torsional moments as well as to gradients in bending moments. In the present application, the thickness t_{bone} of the cylindrical shell is always constant, and the axial-circumferential shear stresses σ_{xs} are considered as not significantly varying over this thickness, so that σ_{xs} is uniquely related to the shear flow F_{xs} , *via*

$$F_{xs} = t_{bone}\sigma_{xs}, \quad (24)$$

whereby the suffix “ s ” relates to the arc length running along the midsurface of the cylindrical shell of thickness t_{bone} , see Figure 2. Such shear stresses may arise from torsional loading, as described further below in Section 2.5,

and from gradients in axial normal stresses, which in the present case stem from various sources, as described in Sections 2.3.2–2.3.4. The coupling between shear stresses and axial normal stresses results from the following specialized form of the 3D local equilibrium condition [15]

$$\frac{\partial \sigma_{xx}}{\partial x} + \frac{\partial \sigma_{xs}}{\partial s} = 0 \quad (25)$$

where the shear stress component along the cylindrical circle is related to the Cartesian shear stress components *via*

$$\sigma_{xy} = -\sigma_{xs} \sin \gamma \quad (26)$$

$$\sigma_{xz} = \sigma_{xs} \cos \gamma \quad (27)$$

and where the gradients of the axial normal stresses will be, in the following, determined from Eqs. (5)–(7). These gradients arise from changes of internal forces, from changes of cross-sectional geometrical properties (areas and area moments), as well as from changes of mechanical properties (values for Young's modulus).

2.3.2. Axial gradients of normal stresses due to bending around *y*-axis

As regards the gradients of axial normal stress due to bending around the *y*-axis, Eq. (6), together with Eq. (3), implies that

$$\frac{\partial \sigma_{xx}^{M_y}}{\partial x} = \left(\frac{\partial \sigma_{xx}^{M_y}}{\partial x} \right)^{dM_y} + \left(\frac{\partial \sigma_{xx}^{M_y}}{\partial x} \right)^{dA} + \left(\frac{\partial \sigma_{xx}^{M_y}}{\partial x} \right)^{dE} \quad (28)$$

where new expressions for axial normal stress gradients arising from a gradient of the bending moment around the *y*-axis, from gradients of bone- and implant-specific cross-sectional areas and area moments, and from a gradient in the elastic modulus have been introduced. In more detail, in Eq. (28), the normal stress gradients arising from a change in the bending moment are given by the following mathematical expression

$$\left(\frac{\partial \sigma_{xx}^{M_y}}{\partial x} \right)^{dM_y} = \frac{E(x, s)}{E_{bone}} \frac{z(s) S_z}{I_{y, bone}(x) + I_{y, imp}(x) (E_{imp}/E_{bone})} \quad (29)$$

with $E(x, s)$ according to Eq. (23). Moreover, in Eq. (28), the normal stress gradients arising from changes in the cross-sectional geometrical properties are given by the following mathematical expression

$$\begin{aligned} \left(\frac{\partial \sigma_{xx}^{M_y}}{\partial x} \right)^{dA} &= -\frac{E(x, s)}{E_{bone}} \frac{z(s) M_y(x)}{[I_{y, bone}(x) + I_{y, imp}(x) (E_{imp}/E_{bone})]^2} \times \\ &\times \frac{dI_{y, bone}(x)}{dx} \left[1 - \frac{E_{imp}}{E_{bone}} \right] \end{aligned} \quad (30)$$

with the gradient of the second-order area moment reading as

$$\begin{aligned} \frac{dI_{y, bone}(x)}{dx} &= -\frac{dI_{y, imp}(x)}{dx} \\ &= \frac{x}{2} [(R_{bone})^4 - (R_{bone} - t_{bone})^4] \times \\ &\times \left(\frac{1 - \cos \left[2 \arcsin \left[\frac{\sqrt{(R_{imp})^2 - x^2}}{(R_{bone} - t_{bone})/2} \right] \right]}{(R_{bone} - t_{bone})/2} \sqrt{(R_{imp})^2 - x^2} \sqrt{1 - \frac{(R_{imp})^2 - x^2}{(R_{bone} - t_{bone})^2}} \right) \end{aligned} \quad (31)$$

Finally, in Eq. (28), the normal stress gradients arising from a change in the elastic modulus are given by the following mathematical expression

$$\left(\frac{\partial \sigma_{xx}^{M_y}}{\partial x} \right)^{dE} = \frac{\partial E(x, s)}{\partial x} \frac{1}{E_{bone}} \frac{z(s) M_y(x)}{I_{y, bone}(x) + \frac{E_{imp}}{E_{bone}} I_{y, imp}(x)} \quad (32)$$

whereby the gradient of the mechanical properties follows from Eq. (23), and consequently, it reads as

$$\begin{aligned} \frac{\partial E(x, s)}{\partial x} &= \frac{d\gamma_{int}(x)}{dx} \left(R_{bone} - \frac{t_{bone}}{2} \right) (E_{imp} - E_{bone}) \times \\ &\left\{ \delta \left[s - \gamma_{int}(x) \times \left(R_{bone} - \frac{t_{bone}}{2} \right) \right] \right. \\ &+ \delta \left[s - [\pi - \gamma_{int}(x)] \times \left(R_{bone} - \frac{t_{bone}}{2} \right) \right] \\ &+ \delta \left[s - [\pi + \gamma_{int}(x)] \times \left(R_{bone} - \frac{t_{bone}}{2} \right) \right] \\ &\left. + \delta \left[s - [2\pi - \gamma_{int}(x)] \times \left(R_{bone} - \frac{t_{bone}}{2} \right) \right] \right\} \end{aligned} \quad (33)$$

In Eq. (33), δ denotes the Dirac delta function, which is the derivative of the Heaviside function; $\delta(\xi = 0) = +\infty$, $\delta(\xi \neq 0) = 0$ and $\int_{-\infty}^{\infty} \delta(\xi) ds = 1$. Moreover, in Eq. (33), it was also considered that

$$\frac{d\gamma_{int}(x)}{dx} = -\frac{x}{\sqrt{(R_{imp})^2 - x^2} \sqrt{1 - \frac{(R_{imp})^2 - x^2}{(R_{bone} - t_{bone})^2}}} \quad (34)$$

2.3.3. Axial gradients of normal stresses due to bending around *z*-axis

As regards the gradients of axial normal stress due to bending around the *z*-axis, Eq. (7), together with Eq. (3), implies that

$$\frac{\partial \sigma_{xx}^{M_z}}{\partial x} = \left(\frac{\partial \sigma_{xx}^{M_z}}{\partial x} \right)^{dM_z} + \left(\frac{\partial \sigma_{xx}^{M_z}}{\partial x} \right)^{dA} + \left(\frac{\partial \sigma_{xx}^{M_z}}{\partial x} \right)^{dE} \quad (35)$$

with new expressions analogous to those introduced below Eq. (28). In more detail, in Eq. (35), the normal stress gradients arising from a change of the bending moment are given by the following mathematical expression

$$\left(\frac{\partial \sigma_{xx}^{M_z}}{\partial x} \right)^{dM_z} = \frac{E(x, s)}{E_{bone}} \frac{y(s) S_y}{I_{z, bone}(x) + I_{z, imp}(x) (E_{imp}/E_{bone})} \quad (36)$$

with $E(x, s)$ according to Eq. (23). Moreover, in Eq. (35), the normal stress gradients arising from changes in the cross-sectional geometrical properties are given by the following mathematical expression

$$\begin{aligned} \left(\frac{\partial \sigma_{xx}^{M_z}}{\partial x} \right)^{dA} &= \frac{E(x, s)}{E_{bone}} \frac{y(s) M_z(x)}{[I_{z, bone}(x) + I_{z, imp}(x) (E_{imp}/E_{bone})]^2} \times \\ &\times \frac{dI_{z, bone}(x)}{dx} \left[1 - \frac{E_{imp}}{E_{bone}} \right] \end{aligned} \quad (37)$$

with the gradient of the second-order area moment reading as

$$\begin{aligned}
\frac{dI_{z,bone}(x)}{dx} &= -\frac{dI_{z,imp}(x)}{dx} \\
&= \frac{x}{2} \left[(R_{bone})^4 - (R_{bone} - t_{bone})^4 \right] \times \\
&\quad \times \left[(R_{bone} - \frac{t_{bone}}{2}) \sqrt{1 - \frac{(R_{imp})^2 - x^2}{(R_{bone} - \frac{t_{bone}}{2})^2}} \right]^{-1} \times \\
&\quad \times \left(\frac{2 - \frac{(R_{imp})^2 - x^2}{(R_{bone} - \frac{t_{bone}}{2})^2}}{\sqrt{(R_{imp})^2 - x^2}} - \frac{\sqrt{(R_{imp})^2 - x^2}}{(R_{bone} - \frac{t_{bone}}{2})^2} \right)
\end{aligned} \quad (38)$$

Finally, in Eq. (35), the normal stress gradients arising from a change in the elastic modulus are given by the following mathematical expression

$$\left(\frac{\partial \sigma_{xx}^{M_z}}{\partial x} \right)^{dE} = -\frac{\partial E(x,s)}{\partial x} \frac{1}{E_{bone}} \frac{y(s)M_z(x)}{I_{z,bone}(x) + \frac{E_{imp}}{E_{bone}} I_{z,imp}(x)} \quad (39)$$

with the gradient of the mechanical properties as shown in Eq. (33), together with Eq. (34).

2.3.4. Axial gradients of normal stresses due to axial loading

As regards the gradients of axial normal stress due to axial force, Eq. (5) implies that

$$\left(\frac{\partial \sigma_{xx}^N}{\partial x} \right) = \left(\frac{\partial \sigma_{xx}^N}{\partial x} \right)^{dA} + \left(\frac{\partial \sigma_{xx}^N}{\partial x} \right)^{dE} \quad (40)$$

with the new expression analogous to those introduced below Eqs. (28) and (35). In Eq. (40), the normal stress gradients arising from changes in the cross-sectional geometrical properties are given by the following mathematical expression

$$\begin{aligned}
\left(\frac{\partial \sigma_{xx}^N}{\partial x} \right)^{dA} &= -\frac{E(x,s)}{E_{bone}} \frac{N(x)}{\left[A_{bone}(x) + A_{imp}(x)(E_{imp}/E_{bone}) \right]^2} \times \\
&\quad \times \frac{dA_{bone}(x)}{dx} \left[1 - \frac{E_{imp}}{E_{bone}} \right]
\end{aligned} \quad (41)$$

with the gradient of the area with x reading as

$$\begin{aligned}
\frac{dA_{bone}(x)}{dx} &= -\frac{dA_{imp}(x)}{dx} \\
&= \frac{4 t_{bone} x}{\sqrt{(R_{imp})^2 - x^2} \sqrt{1 - \frac{(R_{imp})^2 - x^2}{(R_{bone} - \frac{t_{bone}}{2})^2}}}
\end{aligned} \quad (42)$$

Moreover, in Eq. (40), the normal stress gradients arising from a change in the elastic modulus are given by the following mathematical expression

$$\left(\frac{\partial \sigma_{xx}^N}{\partial x} \right)^{dE} = \frac{\partial E(x,s)}{\partial x} \frac{1}{E_{bone}} \frac{N(x)}{A_{bone}(x) + A_{imp}(x)(E_{imp}/E_{bone})} \quad (43)$$

with the gradient of the mechanical properties as shown in Eq. (33), together with Eq. (34).

2.4. Shear stresses from circumferential integration of normal stress gradients

2.4.1. Local equilibrium conditions fulfilled by different stress portions

The local equilibrium conditions according to Eq. (25) are not only required to hold for the entire stress state prevailing at a particular location in the bone-implant structure, but also for individual stress portions making up the total stress, according to Eqs. (28), (35), and (40). As regards the stress portions associated with bending around the y -axis and changes in the corresponding bending moment, local equilibrium according to Eq. (25) implies the following circumferential gradients of shear stresses.

$$\left(\frac{\partial \sigma_{xs}^{M_y}}{\partial s} \right)^{dM_y} = -\left(\frac{\partial \sigma_{xx}^{M_y}}{\partial x} \right)^{dM_y} \quad (44)$$

As regards the stress portions associated with bending around the z -axis and changes in the corresponding bending moment, local equilibrium according to Eq. (25) implies the following circumferential gradients of shear stresses.

$$\left(\frac{\partial \sigma_{xs}^{M_z}}{\partial s} \right)^{dM_z} = -\left(\frac{\partial \sigma_{xx}^{M_z}}{\partial x} \right)^{dM_z} \quad (45)$$

As regards the stress portions associated with geometrical and material property changes under bending and axial loading, respectively, local equilibrium according to Eq. (25) implies the following circumferential gradients of shear stresses.

$$\left(\frac{\partial \sigma_{xs}^{M_y}}{\partial s} \right)^{dA+dE} = -\left(\frac{\partial \sigma_{xx}^{M_y}}{\partial x} \right)^{dA} - \left(\frac{\partial \sigma_{xx}^{M_y}}{\partial x} \right)^{dE} \quad (46)$$

$$\left(\frac{\partial \sigma_{xs}^{M_z}}{\partial s} \right)^{dA+dE} = -\left(\frac{\partial \sigma_{xx}^{M_z}}{\partial x} \right)^{dA} - \left(\frac{\partial \sigma_{xx}^{M_z}}{\partial x} \right)^{dE} \quad (47)$$

$$\left(\frac{\partial \sigma_{xs}^N}{\partial s} \right)^{dA+dE} = -\left(\frac{\partial \sigma_{xx}^N}{\partial x} \right)^{dA} - \left(\frac{\partial \sigma_{xx}^N}{\partial x} \right)^{dE} \quad (48)$$

2.4.2. Shear stress distribution arising from an axial gradient of the bending moment around the y -axis

According to Eqs. (44), (29), (23) and (10), the circumferential gradients of shear stresses arising from an axial gradient of the bending moment around the y -axis are given by the following mathematical expression.

$$\begin{aligned}
\left(\frac{\partial \sigma_{xs}^{M_y}}{\partial s} \right)^{dM_y} &= -\frac{S_z}{I_y} \left(R_{bone} - \frac{t_{bone}}{2} \right) \times \sin \left[\frac{s}{R_{bone} - \frac{t_{bone}}{2}} \right] \times \\
&\quad \times \frac{1}{E_{bone}} \left[E_{imp} - (E_{imp} - E_{bone}) \times \right. \\
&\quad \left. \times \{ H(\xi_1) - H(\xi_2) + H(\xi_3) - H(\xi_4) \} \right]
\end{aligned} \quad (49)$$

where we introduced the following abbreviations for the arguments of the Heaviside function

$$\xi_1 = s - \gamma_{int}(x) \times \left(R_{bone} - \frac{t_{bone}}{2} \right) \quad (50)$$

$$\xi_2 = s - \left[\pi - \gamma_{int}(x) \right] \times \left(R_{bone} - \frac{t_{bone}}{2} \right) \quad (51)$$

$$\xi_3 = s - \left[\pi + \gamma_{int}(x) \right] \times \left(R_{bone} - \frac{t_{bone}}{2} \right) \quad (52)$$

$$\xi_4 = 2\pi - \gamma_{int}(x) \times \left(R_{bone} - \frac{t_{bone}}{2} \right) \quad (53)$$

as well as a “composite second-order area moment around the y -axis” of the form

$$\mathcal{I}_y(x) = I_{y,bone}(x) + I_{y,imp}(x) \frac{E_{imp}}{E_{bone}} \quad (54)$$

Integration of the shear stress gradients of Eq. (49), together with Eqs. (50)–(54), over the circumferential line of the thin-walled bone profile and its extensions into the implant portion of the cross section, yields the shear stresses arising from the axial gradient of the bending moment around the y -axis, in the following form,

$$(\sigma_{xs}^{M_y})^{dM_y}(x, s) = \int_0^s \left(\frac{\partial \sigma_{xs}^{M_y}}{\partial \tilde{s}} \right)^{dM_y}(x, \tilde{s}) d\tilde{s} + (C^{M_y})^{dM_y}(x) \quad (55)$$

Thereby, the integral expression occurring in Eq. (55) reads as

$$\begin{aligned} \left[\int_0^s \left(\frac{\partial \sigma_{xs}^{M_y}}{\partial \tilde{s}} \right)^{dM_y} d\tilde{s} \right](x, s) &= \frac{-S_z}{\mathcal{I}_y(x)} \times \frac{1}{E_{bone}} \left(R_{bone} - \frac{t_{bone}}{2} \right)^2 \times \\ &\times [E_{imp}(1 - \cos[\gamma(s)]) + (E_{imp} - E_{bone}) \times \\ &\times \{ (\cos[\gamma(s)] - \cos[\gamma_{int}(x)]) \times [H(\xi_1) - H(\xi_4)] \times \\ &\times (\cos[\gamma(s)] + \cos[\gamma_{int}(x)]) \times [-H(\xi_2) + H(\xi_3)] \}] \end{aligned} \quad (56)$$

with $\gamma(s)$ according to Eq. (8), $\gamma_{int}(x)$ according to Eq. (11), ξ_1 to ξ_4 according to Eqs. (50)–(53), and \mathcal{I}_y according to Eq. (54). The integration constant $(C^{M_y})^{dM_y}(x)$ occurring in Eq. (55) follows from the condition that shear stresses arising from an axial gradient of the bending moment around the y -axis do not result in a torsional moment (around the x -axis), i.e. from

$$\begin{aligned} (M_x^{M_y})^{dM_y} &= \int_A -z (\sigma_{xy}^{M_y})^{dM_y} + y (\sigma_{xz}^{M_y})^{dM_y} dA \\ &\approx t_{bone} \left(R_{bone} - \frac{t_{bone}}{2} \right) \int_{s=0}^{(R_{bone}-t_{bone}/2)} (\sigma_{xs}^{M_y})^{dM_y} ds = 0 \end{aligned} \quad (57)$$

yielding

$$(C^{M_y})^{dM_y}(x) = \frac{S_z}{\mathcal{I}_y(x)} \frac{(R_{bone} - \frac{t_{bone}}{2})^2}{E_{bone}} [E_{imp} - (E_{imp} - E_{bone}) \cos[\gamma_{int}(x)]] \quad (58)$$

The shear stresses according to Eqs. (55), (56), and (58) also fulfill two conditions in line with Eq. (3), namely that shear stresses arising from bending gradients around the y -axis do not result in shear forces in the y -direction,

$$\begin{aligned} (S_y^{M_y})^{dM_y} &= \int_A (\sigma_{xy}^{M_y})^{dM_y} dA \\ &\approx -t_{bone} \int_{s=0}^{2\pi(R_{bone}-t_{bone}/2)} \sin[\gamma(s)] \times (\sigma_{xs}^{M_y})^{dM_y} ds = 0 \end{aligned} \quad (59)$$

and that the integration, over the cross section, of shear stresses arising from a gradient in the bending moment around the y -axis, yields the shear force in z -direction, i.e.

$$\begin{aligned} (S_z^{M_y})^{dM_y} &= \int_A (\sigma_{xz}^{M_y})^{dM_y} dA \\ &\approx t_{bone} \int_{s=0}^{2\pi(R_{bone}-t_{bone}/2)} \cos[\gamma(s)] \times (\sigma_{xs}^{M_y})^{dM_y} ds \approx S_z \end{aligned} \quad (60)$$

2.4.3. Shear stress distribution arising from an axial gradient of the bending moment around the z -axis

According to Eqs. (45), (36), (23) and (9), the circumferential gradients of shear stresses arising from an axial gradient of the bending moment around the z -axis are given in the following mathematical form

$$\begin{aligned} \left(\frac{\partial \sigma_{xs}^{M_z}}{\partial s} \right)^{dM_z} &= \frac{-S_y}{\mathcal{I}_z(x)} \left(R_{bone} - \frac{t_{bone}}{2} \right) \times \cos \left[\frac{s}{R_{bone} - \frac{t_{bone}}{2}} \right] \times \\ &\times \frac{1}{E_{bone}} [E_{imp} - (E_{imp} - E_{bone}) \times \\ &\times \{ H(\xi_1) - H(\xi_2) + H(\xi_3) - H(\xi_4) \}] \end{aligned} \quad (61)$$

where the abbreviations for the arguments of the Heaviside function still follow Eqs. (50)–(53) and where we introduced a “composite second-order area moment around the z -axis” of the form

$$\mathcal{I}_z(x) = I_{z,bone}(x) + I_{z,imp}(x) \frac{E_{imp}}{E_{bone}} \quad (62)$$

Integration of the shear stress gradients according to Eq. (61), together with Eq. (62), over the circumferential line of the thin-walled bone profile and its extensions into the implant portion of the cross section, yields the shear stresses arising from the axial gradient of the bending moment around z , in the following form,

$$(\sigma_{xs}^{M_z})^{dM_z}(x, s) = \int_0^s \left(\frac{\partial \sigma_{xs}^{M_z}}{\partial \tilde{s}} \right)^{dM_z}(x, \tilde{s}) d\tilde{s} + (C^{M_z})^{dM_z}(x) \quad (63)$$

Thereby, the integral expression occurring in Eq. (63) reads as

$$\begin{aligned} \left[\int_0^s \left(\frac{\partial \sigma_{xs}^{M_z}}{\partial \tilde{s}} \right)^{dM_z} d\tilde{s} \right](x, s) &= \frac{-S_y}{\mathcal{I}_z(x)} \frac{1}{E_{bone}} \left(R_{bone} - \frac{t_{bone}}{2} \right)^2 \times \\ &\times [E_{imp} \sin[\gamma(s)] + (E_{imp} - E_{bone}) \times \\ &\times \{ (\sin[\gamma(s)] - \sin[\gamma_{int}(x)]) \times [-H(\xi_1) + H(\xi_2)] \times \\ &\times (\sin[\gamma(s)] + \sin[\gamma_{int}(x)]) \times [-H(\xi_3) + H(\xi_4)] \}] \end{aligned} \quad (64)$$

with $\gamma(s)$ according to Eq. (8), $\gamma_{int}(x)$ according to Eq. (11), ξ_1 to ξ_4 according to Eqs. (50)–(53), and \mathcal{I}_z according to Eq. (62). The integration constant $(C^{M_z})^{dM_z}(x)$ follows from the condition that shear stresses arising from bending changes around the z -axis do not result in a torsional moment (around the x -axis), i.e. from

$$\begin{aligned}
(M_x^{M_z})^{dM_z} &= \int_A -z (\sigma_{xy}^{M_z})^{dM_z} + y (\sigma_{xz}^{M_z})^{dM_z} dA \\
&\approx t_{bone} \left(R_{bone} - \frac{t_{bone}}{2} \right) \int_0^{(R_{bone}-t_{bone}/2)} (\sigma_{xs}^{M_z})^{dM_z} ds = 0
\end{aligned} \tag{65}$$

yielding

$$(C^{M_z})^{dM_z}(x) = 0 \tag{66}$$

The shear stresses according to Eq. (63), together with Eq. (64) and (66), also fulfill two conditions in line with Eq. (3), namely that shear stresses arising from an axial gradient of the bending moment around the z -axis do not result in shear forces in the z -direction,

$$\begin{aligned}
(S_z^{M_z})^{dM_z} &= \int_A (\sigma_{xz}^{M_z})^{dM_z} dA \\
&\approx -t_{bone} \int_0^{2\pi(R_{bone}-t_{bone}/2)} \sin[\gamma(s)] (\sigma_{xs}^{M_z})^{dM_z} ds = 0
\end{aligned} \tag{67}$$

and that the integration, over the cross section, of the shear stresses arising from an axial gradient of the bending moment around the z -axis yields the shear force in y -direction, i.e.

$$\begin{aligned}
(S_y^{M_z})^{dM_z} &= \int_A (\sigma_{xy}^{M_z})^{dM_z} dA \\
&\approx t_{bone} \int_0^{2\pi(R_{bone}-t_{bone}/2)} \cos[\gamma(s)] (\sigma_{xs}^{M_z})^{dM_z} ds = S_y
\end{aligned} \tag{68}$$

2.4.4. Shear stress distribution arising from axial gradients of cross-sectional properties under bending around the y -axis

According to Eqs. (46), (30), (32), and (10), the circumferential gradients of shear stresses arising from axial gradients of the cross-sectional geometrical properties and of the mechanical properties of a bone-implant compound cross section loaded by a bending moment around the y -axis are given by the following mathematical expression

$$\begin{aligned}
\left(\frac{\partial \sigma_{xy}^{M_y}}{\partial s} \right)^{dA+dE}(x, s) &= \frac{1}{E_{bone}} \frac{M_y(x)z(s)}{\mathcal{I}_y(x)} \times \\
&\times \left[\frac{1}{\mathcal{I}_y(x)} \frac{dI_{y,bone}(x)}{dx} \left[1 - \frac{E_{imp}}{E_{bone}} \right] \times E(x, s) - \frac{\partial E(x, s)}{\partial x} \right] = \\
&= \frac{1}{E_{bone}} \frac{M_y(x)}{\mathcal{I}_y(x)} \left(R_{bone} - \frac{t_{bone}}{2} \right) \sin \left[\frac{s}{R_{bone} - \frac{t_{bone}}{2}} \right] \times \\
&\times \left[\frac{1}{\mathcal{I}_y(x)} \frac{dI_{y,bone}(x)}{dx} \left[1 - \frac{E_{imp}}{E_{bone}} \right] [E_{imp} - (E_{imp} - E_{bone}) \times \right. \\
&\times \{ H(\xi_1) - H(\xi_2) + H(\xi_3) - H(\xi_4) \} \\
&- \frac{d\gamma_{int}(x)}{dx} \left(R_{bone} - \frac{t_{bone}}{2} \right) (E_{imp} - E_{bone}) \times \\
&\times \{ \delta(\xi_1) + \delta(\xi_2) + \delta(\xi_3) + \delta(\xi_4) \}
\end{aligned} \tag{69}$$

with the composite second-order area moment \mathcal{I}_y being given by Eq. (54). Integration of the shear gradients according to Eq. (69), over the circumferential line of the bone profile and its extensions into the implant portions of the cross section, yields the shear stresses arising from the axial gradients of the cross-sectional geometrical properties and of the mechanical properties of a bone-implant compound cross-section loaded by a bending moment around the y -axis as

$$(\sigma_{xs}^{M_y})^{dA+dE}(x, s) = (C^{M_y})^{dA+dE}(x) + \int_0^s \left(\frac{\partial \sigma_{xs}^{M_y}}{\partial \tilde{s}} \right)^{dA+dE}(x, \tilde{s}) d\tilde{s} \tag{70}$$

Thereby, the integral expression in Eq. (70) reads as

$$\begin{aligned}
\left[\int_0^s \left(\frac{\partial \sigma_{xs}^{M_y}}{\partial \tilde{s}} \right)^{dA+dE} d\tilde{s} \right](x, s) &= \frac{M_y}{\mathcal{I}_y(x)} \frac{1}{E_{bone}} \left(R_{bone} - \frac{t_{bone}}{2} \right)^2 \times \\
&\times \left(\frac{1}{\mathcal{I}_y(x)} \frac{dI_{y,bone}(x)}{dx} \left[1 - \frac{E_{imp}}{E_{bone}} \right] \times \right. \\
&\times [-E_{imp} \cos[\gamma(s)] + (E_{imp} - E_{bone}) \times \\
&\times \{ (\cos[\gamma(s)] - \cos[\gamma_{int}(x)]) [H(\xi_1) - H(\xi_4)] \\
&+ (\cos[\gamma(s)] + \cos[\gamma_{int}(x)]) [H(\xi_2) - H(\xi_3)] \} \} \\
&+ (E_{imp} - E_{bone}) \sin[\gamma_{int}(x)] \frac{d\gamma_{int}(x)}{dx} \times \\
&\times \left. \{ -H(\xi_1) - H(\xi_2) + H(\xi_3) + H(\xi_4) \} \right)
\end{aligned} \tag{71}$$

with $\gamma(s)$ according to Eq. (8), $\gamma_{int}(x)$ according to Eq. (11), ξ_1 to ξ_4 according to Eqs. (50)–(53), and \mathcal{I}_y according to Eq. (54). The integration constant $(C^{M_y})^{dA+dE}(x)$ follows from the condition that shear stresses arising from axial gradients of the cross-sectional geometrical properties and of the mechanical properties of a bone-implant compound cross section loaded by a bending moment around the z -axis do neither result in a torsional moment (around the x -axis), i.e. from

$$\begin{aligned}
(M_x^{M_y})^{dA+dE} &= \int_A -z (\sigma_{xy}^{M_y})^{dA+dE} + y (\sigma_{xz}^{M_y})^{dA+dE} dA \\
&\approx t_{bone} \left(R_{bone} - \frac{t_{bone}}{2} \right) \int_0^{2\pi(R_{bone}-t_{bone}/2)} (\sigma_{xs}^{M_y})^{dA+dE} dA = 0
\end{aligned} \tag{72}$$

nor in shear forces in y - and z -direction

$$\begin{aligned}
(S_y^{M_y})^{dA+dE} &= \int_A (\sigma_{xy}^{M_y})^{dA+dE} dA \\
&\approx t_{bone} \int_0^{2\pi(R_{bone}-t_{bone}/2)} \cos[\gamma(s)] (\sigma_{xs}^{M_y})^{dA+dE} ds = 0
\end{aligned} \tag{73}$$

$$\begin{aligned}
(S_z^{M_y})^{dA+dE} &= \int_A (\sigma_{xz}^{M_y})^{dA+dE} dA \\
&\approx t_{bone} \int_0^{2\pi(R_{bone}-t_{bone}/2)} -\sin[\gamma(s)] (\sigma_{xs}^{M_y})^{dA+dE} ds = 0
\end{aligned} \tag{74}$$

yielding

$$\begin{aligned}
(C^{M_y})^{dA+dE}(x) &= \frac{M_y}{\mathcal{I}_y(x)} \frac{1}{E_{bone}} \left(R_{bone} - \frac{t_{bone}}{2} \right)^2 \left[1 - \frac{E_{imp}}{E_{bone}} \right] \times \\
&\times \left[\frac{E_{imp} - E_{bone}}{\mathcal{I}_y(x)} \frac{dI_{y,bone}(x)}{dx} \cos[\gamma_{int}(x)] - E_{bone} \frac{d\gamma_{int}(x)}{dx} \sin[\gamma_{int}(x)] \right]
\end{aligned} \tag{75}$$

2.4.5. Shear stress distribution arising from axial gradients of cross-sectional properties under bending around the z-axis

According to Eqs. (47), (37), (39) and (9), the circumferential gradients of shear stresses arising from axial gradients of the cross-sectional geometrical properties and of the mechanical properties of a bone-implant compound cross section loaded by a bending moment around the z-axis are given by the following mathematical expression

$$\begin{aligned} \left(\frac{\partial \sigma_{xs}^{M_z}}{\partial s} \right)^{dA+dE} (x, s) &= -\frac{1}{E_{bone}} \frac{M_z(x) \gamma(s)}{\mathcal{I}_z(x)} \times \\ &\times \left[\frac{1}{\mathcal{I}_z(x)} \frac{dI_{z,bone}(x)}{dx} \left[1 - \frac{E_{imp}}{E_{bone}} \right] E(x, s) - \frac{\partial E(x, s)}{\partial x} \right] \\ &= -\frac{M_z(x)}{\mathcal{I}_z(x)} \frac{1}{E_{bone}} \left(R_{bone} - \frac{t_{bone}}{2} \right) \cos \left[\frac{s}{R_{bone} - \frac{t_{bone}}{2}} \right] \times \\ &\times \left[\frac{1}{\mathcal{I}_z(x)} \frac{dI_{z,bone}(x)}{dx} \left[1 - \frac{E_{imp}}{E_{bone}} \right] [E_{imp} - (E_{imp} - E_{bone}) \times \right. \\ &\times \{H_1(x, s) - H_2(x, s) + H_3(x, s) - H_4(x, s)\}] \\ &\left. - \frac{d\gamma_{int}(x)}{dx} \left(R_{bone} - \frac{t_{bone}}{2} \right) (E_{imp} - E_{bone}) \times \right. \\ &\left. \times \{ \delta_1(x, s) + \delta_2(x, s) + \delta_3(x, s) + \delta_4(x, s) \} \right] \quad (76) \end{aligned}$$

with the composite second-order area moment \mathcal{I}_z being given by Eq. (62). Integration of the shear stress gradients according to Eq. (76), over the circumferential line of the bone profile and its extensions into the implant portion of the cross section, yields the shear stresses arising from the axial gradients of the cross-sectional geometrical properties and of the mechanical properties of a bone-implant compound cross-section loaded by a bending moment around the z-axis as

$$\left(\sigma_{xs}^{M_z} \right)^{dA+dE} (x, s) = (C^{M_z})^{dA+dE} (x) + \int_0^s \left(\frac{\partial \sigma_{xs}^{M_z}}{\partial \tilde{s}} \right)^{dA+dE} (x, \tilde{s}) d\tilde{s} \quad (77)$$

Thereby, the integral expression in Eq. (77) reads as

$$\begin{aligned} \left[\int_0^s \left(\frac{\partial \sigma_{xs}^{M_z}}{\partial \tilde{s}} \right)^{dA+dE} d\tilde{s} \right] (x, s) &= \frac{M_z(x)}{\mathcal{I}_z(x)} \frac{1}{E_{bone}} \left(R_{bone} - \frac{t_{bone}}{2} \right)^2 \times \\ &\times \left(\frac{1}{\mathcal{I}_z(x)} \frac{dI_{z,bone}(x)}{dx} \left[1 - \frac{E_{imp}}{E_{bone}} \right] \times \right. \\ &\times [-E_{imp} \sin[\gamma(s)] + (E_{imp} - E_{bone}) \times \\ &\times \{ (\sin[\gamma(s)] - \sin[\gamma_{int}(x)]) [H(\xi_1) - H(\xi_2)] \\ &\times + (\sin[\gamma(s)] + \sin[\gamma_{int}(x)]) [H(\xi_3) - H(\xi_4)] \}] \\ &\left. + (E_{imp} - E_{bone}) \cos[\gamma_{int}(x)] \frac{d\gamma_{int}(x)}{dx} \times \right. \\ &\left. \times [H(\xi_1) - H(\xi_2) - H(\xi_3) + H(\xi_4)] \right) \quad (78) \end{aligned}$$

with $\gamma(s)$ according to Eq. (8), $\gamma_{int}(x)$ according to Eq. (11), ξ_1 to ξ_4 according to Eqs. (50)–(53), and \mathcal{I}_y according to Eq. (54). The integration constant $(C^{M_z})^{dA+dE}(x)$ follows from the condition that shear stresses arising from axial gradients in the cross-sectional geometrical properties and of the mechanical properties of

a bone-implant compound cross-section loaded by a bending moment around the z-axis do neither result in a torsional moment (around the x-axis), mathematically reading as

$$\begin{aligned} \left(M_x^{M_z} \right)^{dA+dE} &= \int_A -z (\sigma_{xy}^{M_z})^{dA+dE} + y (\sigma_{xz}^{M_z})^{dA+dE} dA \\ &\approx t_{bone} \left(R_{bone} - \frac{t_{bone}}{2} \right) \int_0^{2\pi(R_{bone}-t_{bone}/2)} (\sigma_{xs}^{M_z})^{dA+dE} ds = 0 \quad (79) \end{aligned}$$

nor in shear forces in y- and z-direction, mathematically reading as

$$\left(S_y^{M_z} \right)^{dA+dE} = \int_A (\sigma_{xy}^{M_z})^{dA+dE} dA \quad (80)$$

$$\approx t_{bone} \int_A \cos[\gamma(s)] (\sigma_{xs}^{M_z})^{dA+dE} ds = 0$$

$$\begin{aligned} \left(S_z^{M_z} \right)^{dA+dE} &= \int_A (\sigma_{xz}^{M_z})^{dA+dE} dA \\ &\approx t_{bone} \int_0^{2\pi(R_{bone}-t_{bone}/2)} -\sin[\gamma(s)] (\sigma_{xs}^{M_z})^{dA+dE} ds = 0 \quad (81) \end{aligned}$$

yielding

$$(C^{M_z})^{dA+dE}(x) = 0 \quad (82)$$

2.4.6. Shear stress distribution arising from axial gradients of cross-sectional properties under axial loading

According to Eqs. (48), (41) and (43), the circumferential gradients of shear stresses arising from axial gradients of the cross-sectional geometrical properties and of the mechanical properties of a bone-implant compound cross section loaded by a constant axial force are given by the following mathematical expression

$$\begin{aligned} \left(\frac{\partial \sigma_{xs}^N}{\partial s} \right)^{dA+dE} (x, s) &= \frac{1}{E_{bone}} \frac{N(x)}{\mathcal{A}(x)} \times \\ &\times \left(\frac{1}{\mathcal{A}(x)} \frac{dA_{bone}(x)}{dx} \left[1 - \frac{E_{imp}}{E_{bone}} \right] [E_{imp} - (E_{imp} - E_{bone}) \times \right. \\ &\times \{H(\xi_1) - H(\xi_2) + H(\xi_3) - H_4(\xi_4)\}] \\ &\times - \frac{d\gamma_{int}(x)}{dx} \left(R_{bone} - \frac{t_{bone}}{2} \right) (E_{imp} - E_{bone}) \times \\ &\left. \times \{ \delta(\xi_1) + \delta(\xi_2) + \delta(\xi_3) + \delta(\xi_4) \} \right) \quad (83) \end{aligned}$$

where we introduced a “composite area” of the form

$$\mathcal{A}(x) = A_{bone}(x) + A_{imp}(x) \frac{E_{imp}}{E_{bone}} \quad (84)$$

Integration of the shear gradients according to Eq. (83), over the circumferential line of the bone profile and its extensions into the implant portion of the cross section, yields the shear stresses arising from the changes in the cross-sectional geometrical properties and in the mechanical properties of a bone-implant compound cross-section loaded by a constant axial force as

$$\left(\sigma_{xs}^N \right)^{dA+dE} (x, s) = (C^N)^{dA+dE} (x) + \int_0^s \left(\frac{\partial \sigma_{xs}^N}{\partial \tilde{s}} \right)^{dA+dE} (x, \tilde{s}) d\tilde{s} \quad (85)$$

Thereby, the integral expression occurring in Eq. (85) reads as

$$\begin{aligned} & \left[\int_0^s \left(\frac{\partial \sigma_{xs}^N}{\partial s} \right)^{dA+dE} ds \right] (x, s) = \frac{N(x)}{\mathcal{A}(x)} \frac{1}{E_{bone}} \times \\ & \times \left(\frac{1}{\mathcal{A}(x)} \frac{dA_{bone}(x)}{dx} \left[1 - \frac{E_{imp}}{E_{bone}} \right] \times \right. \\ & \times [E_{imp} \times s + (E_{imp} - E_{bone}) \times \\ & \times \{-\xi_1 H(\xi_1) + \xi_2 H(\xi_2) - \xi_3 H(\xi_3) + \xi_4 H(\xi_4)\}] \\ & \left. - \frac{d\gamma_{int}(x)}{dx} \left(R_{bone} - \frac{t_{bone}}{2} \right) (E_{imp} - E_{bone}) \times \right. \\ & \left. \times \{H(\xi_1) + H(\xi_2) + H(\xi_3) + H(\xi_4)\} \right) \end{aligned} \quad (86)$$

with $\gamma(s)$ according to Eq. (8), $\gamma_{int}(x)$ according to Eq. (11), ξ_1 to ξ_4 according to Eqs. (50)–(53), and \mathcal{A} according to (84). The integration constant $(C^N)^{dA+dE}(x)$ follows from the condition that shear stresses arising from axial gradients in the cross-sectional geometrical properties and of the mechanical properties of a bone-implant compound cross-section loaded by a bending moment around the z -axis do neither result in a torsional moment (around the x -axis), mathematically reading as

$$\begin{aligned} (M_x^N)^{dA+dE} &= \int_A -z (\sigma_{xy}^N)^{dA+dE} + y (\sigma_{xz}^N)^{dA+dE} dA \\ &\approx t_{bone} \left(R_{bone} - \frac{t_{bone}}{2} \right) \int_0^{2\pi(R_{bone}-t_{bone}/2)} (\sigma_{xs}^N)^{dA+dE} ds = 0 \end{aligned} \quad (87)$$

nor in shear forces in y - and z -direction, mathematically reading as

$$\begin{aligned} (S_y^N)^{dA+dE} &= \int_A (\sigma_{xy}^N)^{dA+dE} dA \\ &\approx t_{bone} \int_0^{2\pi(R_{bone}-t_{bone}/2)} \cos[\gamma(s)] (\sigma_{xs}^N)^{dA+dE} ds = 0 \end{aligned} \quad (88)$$

$$\begin{aligned} (S_z^N)^{dA+dE} &= \int_A (\sigma_{xz}^N)^{dA+dE} dA \\ &\approx \int_0^{2\pi(R_{bone}-t_{bone}/2)} -\sin[\gamma(s)] (\sigma_{xs}^N)^{dA+dE} dA = 0 \end{aligned} \quad (89)$$

yielding

$$\begin{aligned} (C^N)^{dA+dE}(x) &= \frac{-N}{\mathcal{A}(x)} \frac{1}{E_{bone}} \times \left[\frac{E_{bone} \pi + 2(E_{imp} - E_{bone}) \gamma_{int}(x)}{\mathcal{A}(x)} \frac{dA_{bone}(x)}{dx} \right. \\ & \left. \times \left[1 - \frac{E_{imp}}{E_{bone}} \right] - 2(E_{imp} - E_{bone}) \frac{d\gamma_{int}(x)}{dx} \right] = 0 \end{aligned} \quad (90)$$

2.5. Shear stresses arising from torsional loading

As regards shear stresses arising from torsional loading, we adopt the classical modeling approach [18]. Accordingly, the local equilibrium condition for shear stresses $\sigma_{xs}^{M_x}$ arising from a torsional moment M_x reads as

$$\frac{\partial \sigma_{xs}^{M_x}}{\partial s} = 0 \rightarrow \sigma_{xs}^{M_x}(s, x = \text{const.}) = \text{const.} \quad (91)$$

and these shear stresses obey the classical relation ([18], 2011, page 414)

$$\sigma_{xs}^{M_x} = \frac{M_x \left(R_{bone} - \frac{t_{bone}}{2} \right)}{I_p} \quad (92)$$

with the second polar moment of area reading as

$$I_p = \frac{\pi}{2} [(R_{bone})^4 - (R_{bone} - t_{bone})^4] \quad (93)$$

2.6. Higher-order stress average as measure for implant and bone loading

In order to study the effect of design parameter changes, such as the radius or the elastic modulus of the implant, on the stress levels encountered in the bone and implant portions of the femur-implant compound structure, we resort to the concept of higher-order stress averages [21, 22], which have turned out as very useful measures in the context of strength upscaling in micromechanics [23], with applications to bone biomaterials [24], metallic implant materials [25], wood [26, 27], and concrete [28–30]. As concerns appropriate measures for the load bearing capacity, the stress deviator σ_d is a particularly popular choice,

$$\sigma_d = \sigma - \frac{1}{3} \text{tr} \sigma \quad (94)$$

with the corresponding higher-order stress average over the bone and implant portions in a cross section of the organ-implant compound structure being given as [22, 26, 28, 31]

$$\begin{aligned} \mathfrak{s}_{bone} &= \sqrt{\frac{1}{A_{bone}} \int_{A_{bone}} \frac{1}{2} \sigma_d : \sigma_d dA} \\ &\approx \sqrt{\frac{1}{2\pi - 4\gamma_{int}} \left(\int_{\gamma_{int}}^{\pi-\gamma_{int}} \left[(\sigma_{xs})^2 + \frac{(\sigma_{xx})^2}{3} \right] d\gamma + \int_{\pi+\gamma_{int}}^{2\pi-\gamma_{int}} \left[(\sigma_{xs})^2 + \frac{(\sigma_{xx})^2}{3} \right] d\gamma \right)} \end{aligned} \quad (95)$$

$$\begin{aligned} \mathfrak{s}_{imp} &= \sqrt{\frac{1}{A_{imp}} \int_{A_{imp}} \frac{1}{2} \sigma_d : \sigma_d dA} \\ &\approx \sqrt{\frac{1}{4\gamma_{int}} \left(\int_0^{\gamma_{int}} \left[(\sigma_{xs})^2 + \frac{(\sigma_{xx})^2}{3} \right] d\gamma + \int_{\pi-\gamma_{int}}^{\pi+\gamma_{int}} \left[(\sigma_{xs})^2 + \frac{(\sigma_{xx})^2}{3} \right] d\gamma + \int_{2\pi-\gamma_{int}}^{2\pi} \left[(\sigma_{xs})^2 + \frac{(\sigma_{xx})^2}{3} \right] d\gamma \right)} \end{aligned} \quad (96)$$

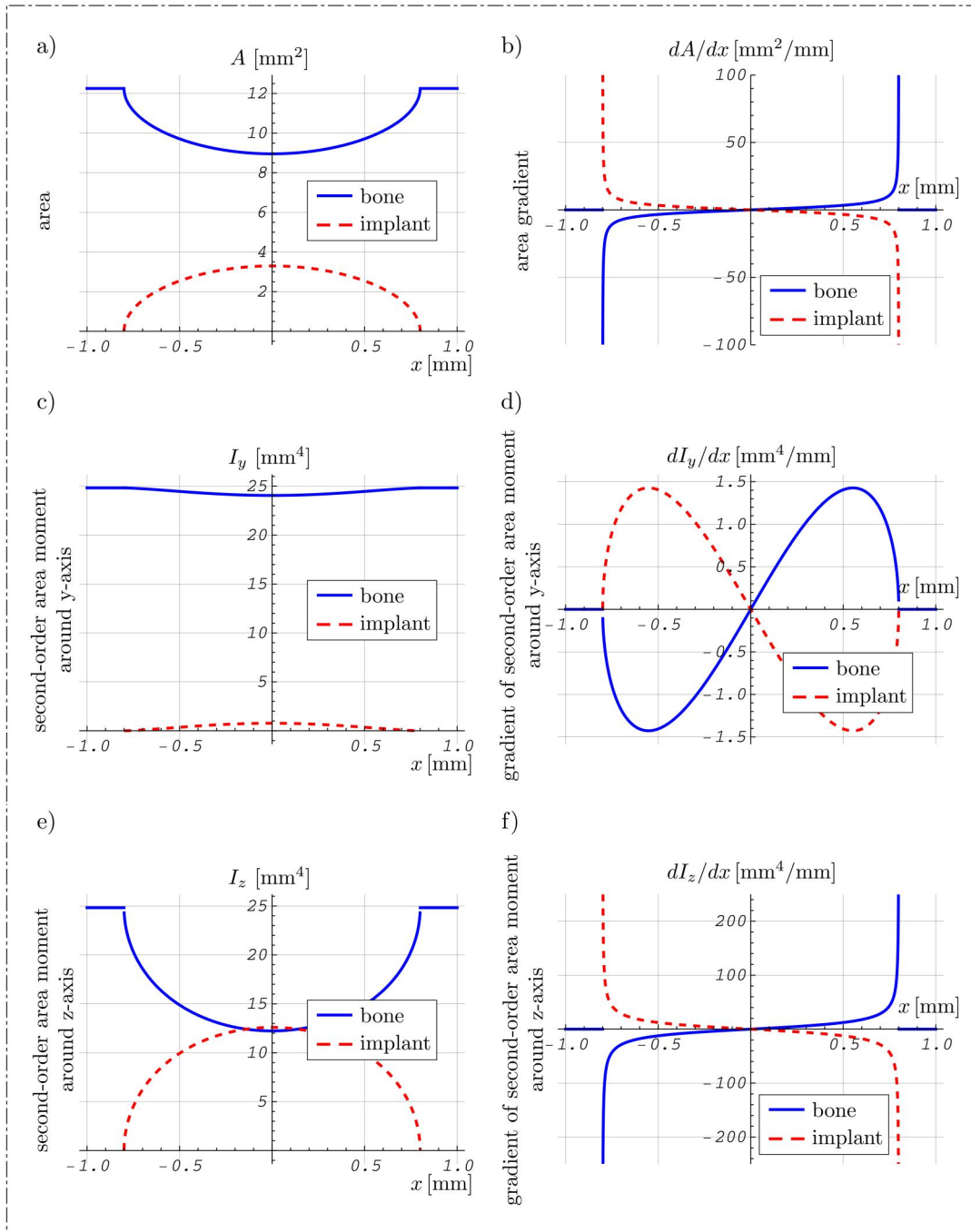


Figure 4. Typical trends of cross-sectional area A and area moments I_y and I_z along bone shaft axis around the magnesium implant; i.e. for the geometrical conditions encountered in [5], see Table 1: Distributions of (a) cross-sectional area, (b) axial gradient of cross-sectional area, (c) second-order area moment around y -axis, (d) axial gradient of second-order area moment around y -axis, (e) second-order area moment around z -axis, and (f) axial gradient of second-order area moment around z -axis.

with the stress deviator according to Eq. (94) and the tress tensor following Eq. (1), together with Eqs. (26) and (27), whereby the normal and shear stress components result from summing up contributions from normal forces, bending and torsional moments, and those from changes in bending moments and cross-sectional as well as material properties

$$\sigma_{xx} = \sigma_{xx}^N + \sigma_{xx}^{M_y} + \sigma_{xx}^{M_z} \quad (97)$$

$$\sigma_{xs} = (\sigma_{xs}^N)^{dA+dE} + (\sigma_{xs}^{M_y})^{dA+dE} + (\sigma_{xs}^{M_z})^{dA+dE} + (\sigma_{xs}^{M_y})^{dM_y} + (\sigma_{xs}^{M_z})^{dM_z} + \sigma_{xs}^{M_z} \quad (98)$$

3. Illustration of geometrical properties and characteristic stress states

While the second-order area moment around the y -axis, of the bone portions of the composite cross sections is hardly influenced by the presence of the implant, see Figure 4(c), this presence reduces the cross-sectional bone area by up to 25 %, see Figure 4(a), and the second-order bone area moment around the z -axis by around 50 %, see Figure 4(e). According to Eqs. (5)–(7), we therefore expect only slight to moderate effects of the presence of the implant on the axial

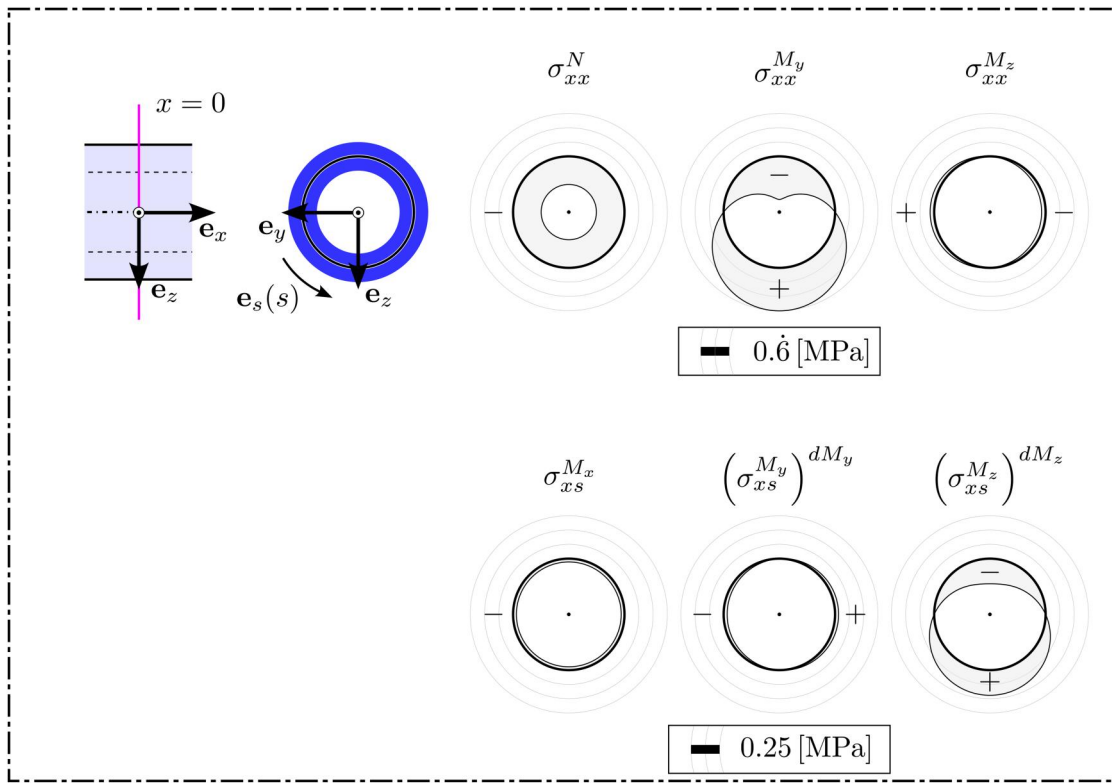


Figure 5. Normal and shear stresses arising from the loading given in Eq. (2), for the “classical case” of a hollow cylindrical beam without implant ($R_{imp}=0$).

normal stresses, as compared to the situation without implant, illustrated in Figure 5. At the same time, the axial gradients of the cross-sectional area and of the second-order area moment around the z -axis exhibit singularities at the positions $x = \pm R_{imp}$, see Figure 4(b,f). According to Eqs. (5)–(7), together with Eq. (25), this lets us expect shear stresses which tend toward infinity at these very locations, to be discussed in more detail in the next paragraph.

In quantitative and illustrative terms, the stress distributions across the femur-implant structure can be described as follows: The normal stresses arising from axial loading are scaled by the ratio of the elastic moduli of bone and implant, respectively, irrespective of the thickness of the implant portion in the composite cross sections, see the stress distributions in the third column of Figure 6, as an illustration of the evaluation of Eq. (5) for the loading defined by Eq. (2). A similar scaling is observed for the normal stresses due to bending moments around y - and z -axis, respectively. These bending moments, however, do not only scale with the modulus ratio, but also with the distance from the geometrical center of the composite cross section, see stress distributions in the fourth and fifth column of Figure 6, as illustrations of Eqs. (6) and (7) for the loading defined by Eq. (2). In quantitative terms, the loading given through Eq. (2) results in normal stresses due to bending around the y -axis, i.e. the axis parallel to the implant axis, which dominate in the bone portion of the compound structure, while the normal stresses due to (compressive) axial normal force dominate in the implant portion. By comparison, the normal stresses due to bending around the z -axis

are significantly smaller. However, gradients of the bending moment around the z -axis along the long axis of the bone shaft, i.e. along the x -axis, result in significant axial-circumferential shear stresses, see the stress distributions in the fifth column of Figure 7, as an illustration of Eq. (63), together with Eqs. (64) and (66), for the loading defined by Eq. (2). These shear stresses are much larger in magnitude than those arising from torsional loading, see the stress distributions in the third column of Figure 7, as an illustration of Eq. (92), together with Eq. (93), for the loading defined by Eq. (2). The shear stresses due to changing bending moments around the z axis are also much larger than those arising from the change of bending moments around the y -axis along the long axis of the bone shaft, see the stress distributions in the fourth column of Figure 7, as an illustration of Eq. (55), together with Eqs. (56) and (58), for the loading defined by Eq. (2). Still, along the implant-bone interface in the periphery of the implant, i.e. where $x \approx \pm R_{imp}$, the absolute value of all these shear stresses is significantly exceeded by the magnitude of the shear stresses arising from changes along the bone shaft axis, in area, in area moment, as well as in elastic modulus, of the bone- and implant-specific cross-sectional portions, respectively; see the first and second column of Figure 8. These shear stresses are mainly triggered by the axial normal force, see third column of Figure 8, and they are also due to bending around the z -axis, see fifth column of Figure 8, while bending around the y -axis plays a subordinate role, see fourth column of Figure 8. Being zero at the implant center, $x = 0$, these cross-sectional-property-driven shear stresses build up

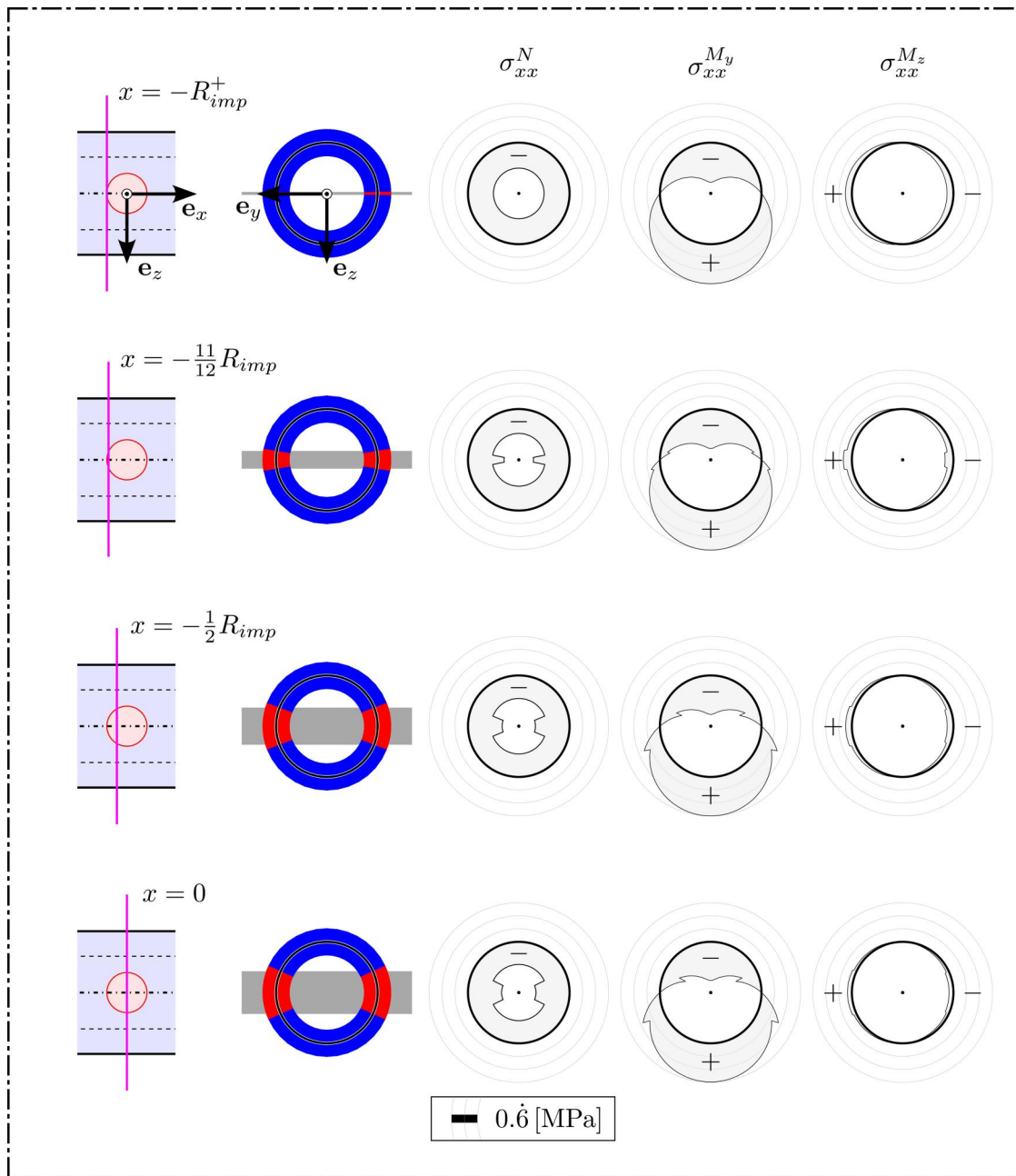


Figure 6. Axial normal stresses σ_{xx} arising from normal force (N) and from bending moments around the y - and z -axis (M_y and M_z), in different cross sections through the implant (red) and the adjacent bone portions (blue); $-R_{imp}^+$ refers to the limit of reaching the implant radius from the right.

fairly quickly when following the bone-implant interface at the bone side, along the x -axis, see Figure 9. Concerning the influence of design parameters on the stress levels in the implant-compound structure as quantified in terms of Eqs. (95) and (96), the implant-to-bone radius ratio plays an only minor role (see Figure 10), while deviations of the implant-to-bone modulus ratio from the value of one are of primary importance (see Figure 11).

4. Discussion

In this paper, we developed a new analytical mechanics model for a bone-implant structure consisting of a femoral

shaft and a cylindrical implant positioned orthogonal to the long-bone axis of the femoral shaft: Normal stresses following from classical composite beam theory were combined with local equilibrium conditions, so as to derive, based on differentiation and integration steps in space, closed-form analytical expressions for shear stress fields throughout the considered preclinical animal model. The most striking feature which distinguishes the results of this new model from the results of classical beam theory applied to the femoral bone shaft only, are the high shear stresses occurring close to the implant surface generators intersecting the bone shaft axis. If these stress singularities are a realistic reflection of dramatic stress redistributions

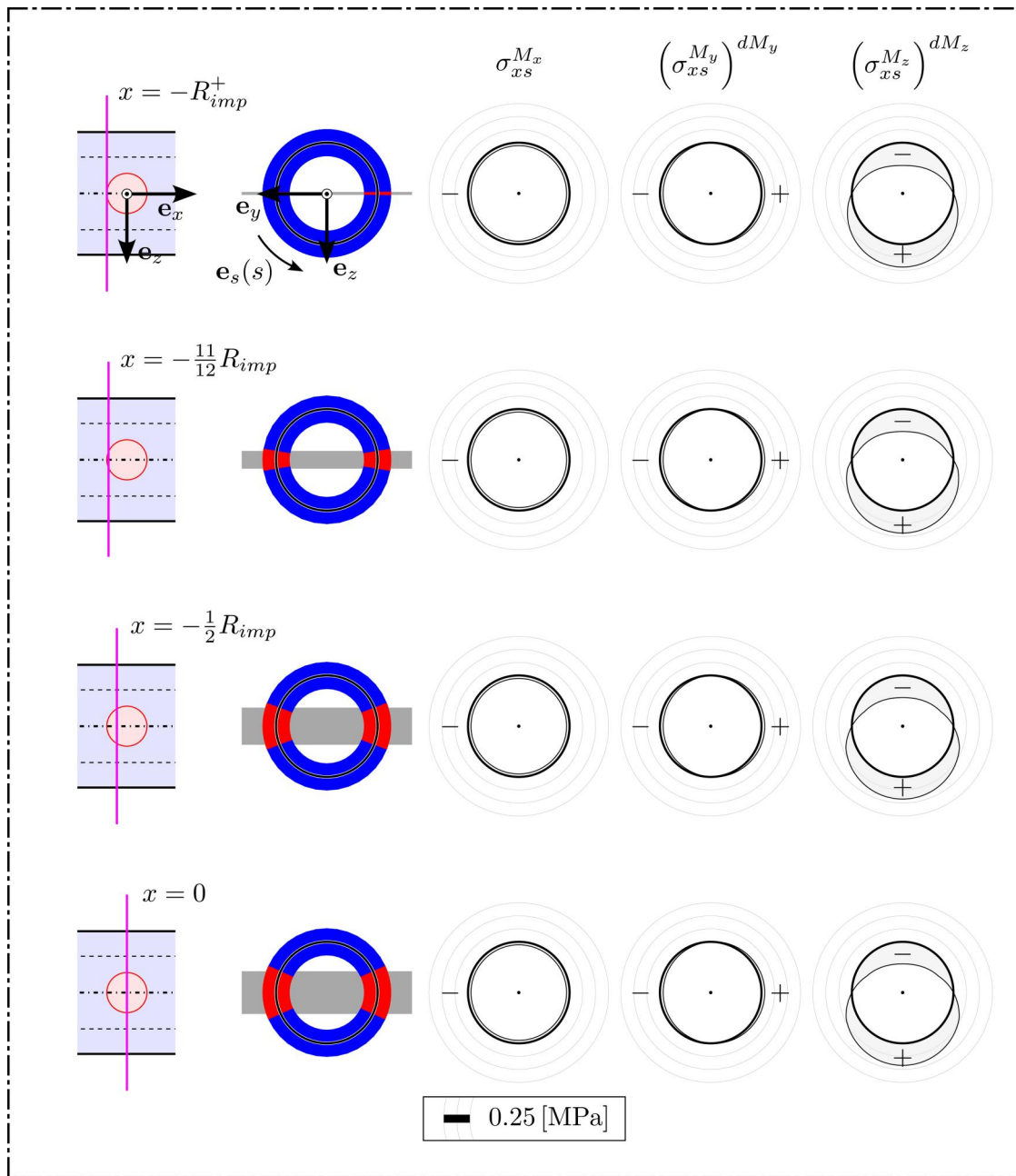


Figure 7. Axial-circumferential shear stresses σ_{xs} arising from torsional moments (M_x), and from changes in the bending moments (dM_y and dM_z), in different cross sections through the implant (red) and the adjacent bone portions (blue); $-R_{imp}^+$ refers to the limit of reaching the implant radius from the right.

due to implantation, then they would – according to the observations in mechanobiology – cause significant bone remodeling and transformation events in the aforementioned bone regions adjacent to the implant. And indeed, such transformation events are clearly evidenced by tensor tomograms of the surroundings of magnesium implants in murine femora, see Figure 12.

These remodeling processes – namely reorientation of bone fibril, away from the bone axis direction, toward a direction which is orthogonal to the bone axis – occur close to the bone-implant interface regions adjacent to the bone axis, and diminish with increasing distance from this axis. Hence, the remodeling events are closely related to

the very high shear stresses proposed by our new model, and in this sense, the experimental evidence underlines the principal relevance of the modeling approach. In more detail, the probable mechanobiological phenomena may be sketched as follows: At first, high stress concentrations result in “overuse” of bone, and in local demineralization, delamination, and disintegration of the extracellular nanocomposite, i.e. to bone resorption [32], followed by the process of new bone formation, which starts with the deposition of fibrils in a non-mineralized ground substance [33]. If such a material system is subjected to shear, the fibrils do not only undergo deformations, but also rotational rigid body motions, as was shown by dedicated

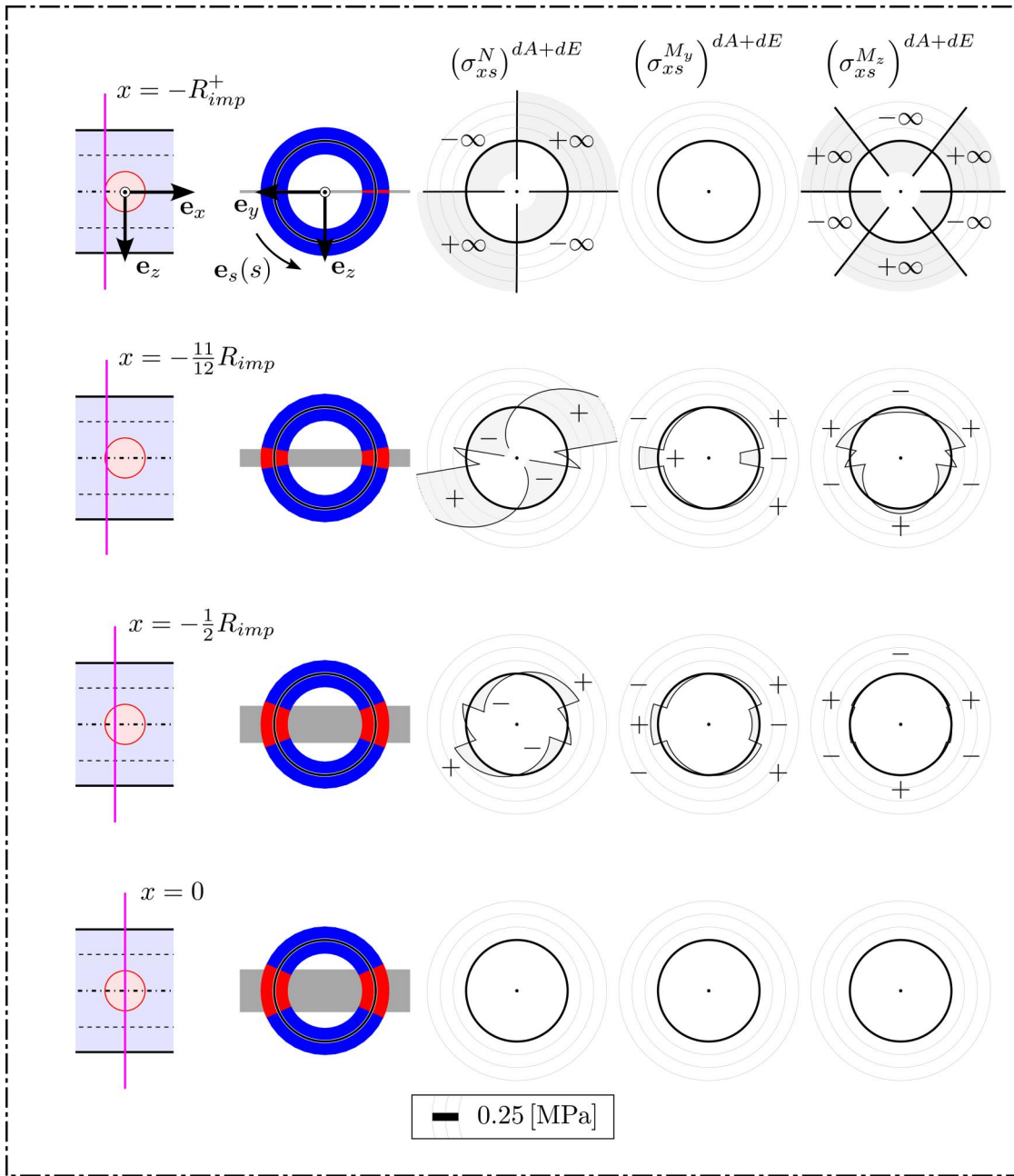


Figure 8. Axial-circumferential shear stresses arising from changes in the cross-section along the beam axis, together with loading in terms of axial force and bending moments, in different cross sections through the implant (red) and the adjacent bone portions (blue); $-R_{imp}^+$ refers to the limit of reaching the implant radius from the right.

micromechanical models based on Eshelby problems formulated in rate form, together with thermodynamically consistent hypoelastic material modeling at the phase level [34, 35]. These rotated fibrils then undergo the well-known vesicle-driven mineralization process [36–38], which affects both intrafibrillar and extrafibrillar spaces [39, 40]. Thereby, however, the extrafibrillar mineral portion comprises not only the majority of the mineral crystals [41–43], but also appears as key driver of important mechanical properties of bone, such as its (visco-)elasticity [44–46] and strength [47, 48].

Finally, our approach is naturally characterized by several limitations which may motivate further studies in the

future. This naturally relates to geometrical objects exceeding the simple nature of circular cylinders; but, probably more interestingly, to more advanced beam theory approaches, as may be motivated in the following way: The current differentiation and integration of the normal stresses arising from classical composite beam theory result in partially infinitely large shear stresses. While the occurrence of “very large” shear stresses makes great sense in terms of mechanobiology, as discussed further above, these singularities can obviously reflect quantitatively these very large stresses, i.e. they cannot provide numerical values for these stresses. If such a quantitative analysis is desired, the proposed modeling approach needs

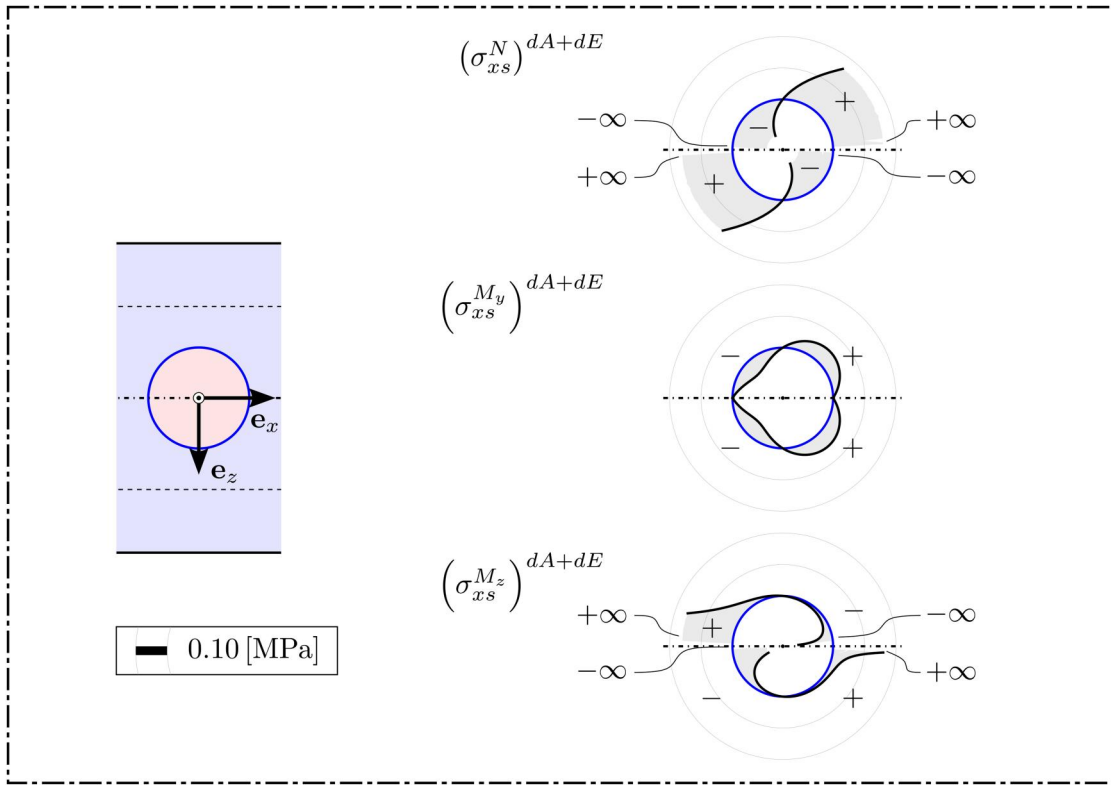


Figure 9. Distribution along the bone-side of the bone-implant interface, of shear stresses arising from cross-sectional changes together with loading by axial force or bendings moments around y - or z -axis.

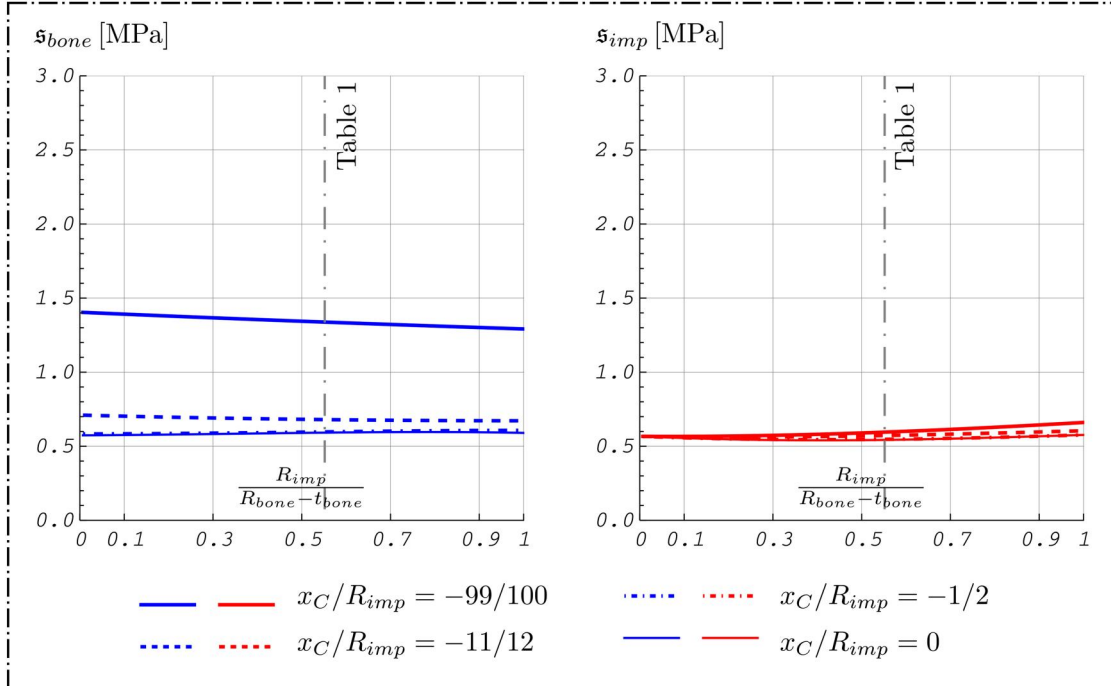


Figure 10. Higher-order stress averages s_{bone} and s_{imp} associated with selected cross-sections, as functions of R_{imp} , t_{bone} , E_{imp} , and E_{bone} according to Table 1.

further refinement. Actually, the occurrence of very high shear stresses, together with very large strain gradients, may propose, as an interesting future step, the consideration of corresponding shear strains in the context of formulating equilibrium conditions at the level of the overall

composite beam. Therefore, the virtual fields as given in Eq. (A1), would need to undergo extensions in their degrees of freedom, so as to allow for significant virtual shear rate gradients [49, 50], which follow the geometrical features of the composite cross section. This may lead to

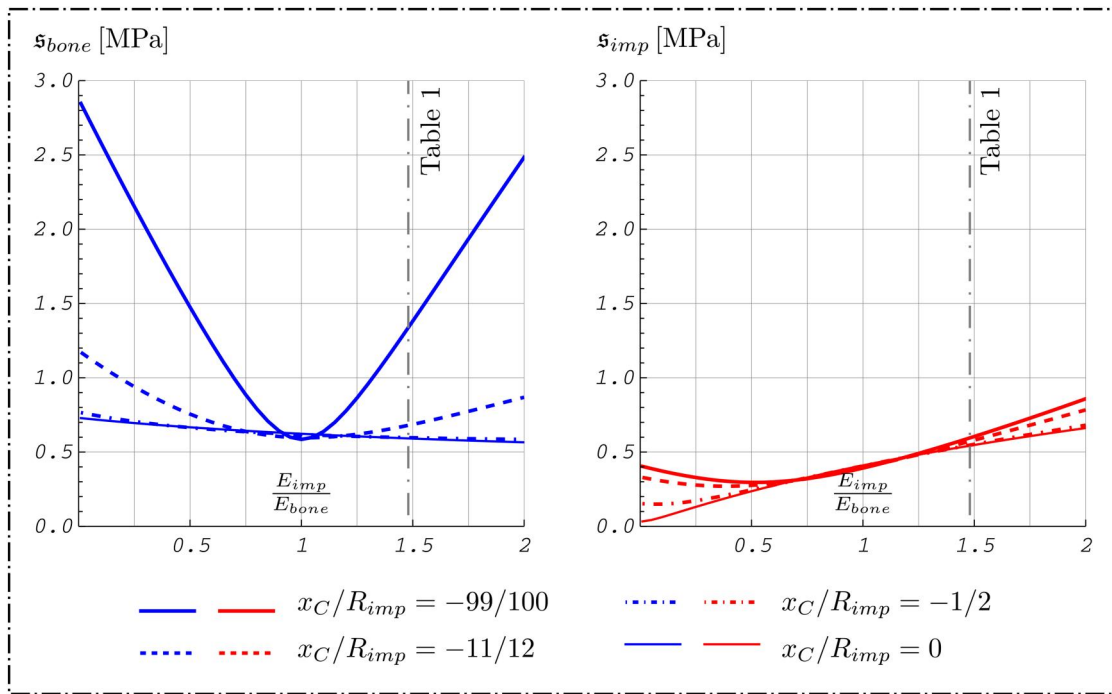


Figure 11. Higher-order stress averages \bar{s}_{bone} and \bar{s}_{imp} associated with selected cross-sections, as functions of R_{imp} , R_{bone} , t_{bone} , and E_{bone} according to Table 1.

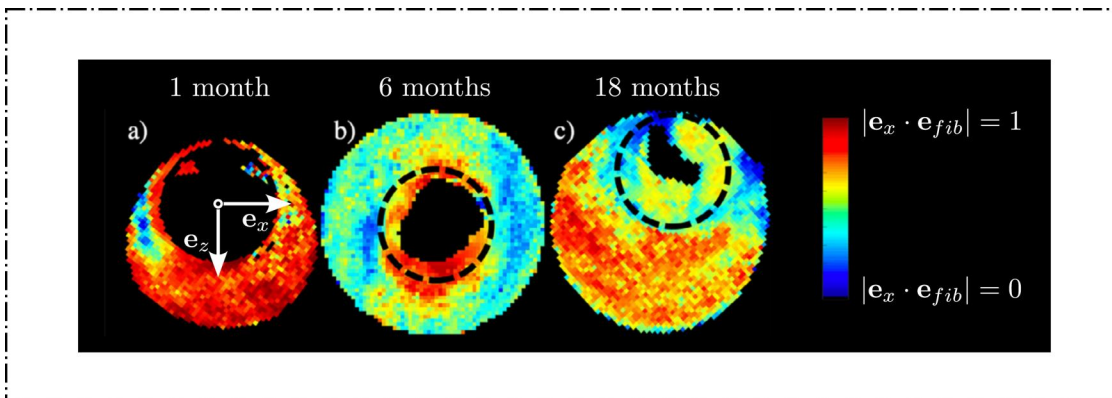


Figure 12. Alignment of bone fibril orientation \mathbf{e}_{fb} with the femoral axis, in terms of an inner product, as reported in [5]; adaptation of Figure 5 of the aforementioned reference, under license CC by 4.0.

additional developments and applications in the field of shear-compliant composite beam theories, as they have been very successfully developed in the context of lightweight and aerospace engineering [51, 52].

Disclosure statement

No potential conflict of interest was reported by the authors.

Funding

This research was funded in whole or in part by the Austrian Science Fund (FWF) [grant DOI: 10.55776/I4409]. L.P. and C.H. acknowledge TU Wien Bibliothek for financial support through its Open Access Funding Programme. Furthermore, T.G. acknowledges funding by the

European Union, European Research Council Horizon Europe, TexTOM [grant no. 101041871]. Views and opinions expressed are those of the author(s) only and do not necessarily reflect those of the European Union or the European Research Council. Neither the European Union nor the granting authority can be held responsible for them.

References

- [1] P. Mukherjee, S. Roy, D. Ghosh, and S.K. Nandi, Role of animal models in biomedical research: a review, *Lab. Anim. Res.*, vol. 38, no. 1, pp. 18, 2022. DOI: 10.1186/s42826-022-00128-1.
- [2] S.K. Doke and S.C. Dhawale, Alternatives to animal testing: a review, *Saudi Pharm. J.*, vol. 23, no. 3, pp. 223–229, 2015. DOI: 10.1016/j.jsps.2013.11.002.
- [3] C. Castellani, R.A. Lindtner, P. Hausbrandt, E. Tschegg, S.E. Stanzl-Tschegg, G. Zanoni, S. Beck, and A. Weinberg, Bone-

- implant interface strength and osseointegration: biodegradable magnesium alloy versus standard titanium control, *Acta Biomater.*, vol. 7, no. 1, pp. 432–440, 2011. DOI: [10.1016/j.actbio.2010.08.020](https://doi.org/10.1016/j.actbio.2010.08.020).
- [4] T.A. Grünewald, H. Rennhofer, B. Hesse, M. Burghammer, S.E. Stanzl-Tschegg, M. Cotte, J.F. Löffler, A. Weinberg, and H.C. Lichtenegger, Magnesium from bioresorbable implants: distribution and impact on the nano- and mineral structure of bone, *Biomaterials*, vol. 76, pp. 250–260, 2016. DOI: [10.1016/j.biomaterials.2015.10.054](https://doi.org/10.1016/j.biomaterials.2015.10.054).
- [5] M. Liebi, V. Lutz-Bueno, M. Guizar-Sicairos, B.M. Schönbauer, J. Eichler, E. Martinelli, J.F. Löffler, A. Weinberg, H. Lichtenegger, and T.A. Grünewald, 3D nanoscale analysis of bone healing around degrading mg implants evaluated by x-ray scattering tensor tomography, *Acta Biomater.*, vol. 134, pp. 804–817, 2021. DOI: [10.1016/j.actbio.2021.07.060](https://doi.org/10.1016/j.actbio.2021.07.060).
- [6] A. Hermann, A. Shojaei, D. Steglich, D. Höche, B. Zeller-Plumhoff, and C.J. Cyron, Combining peridynamic and finite element simulations to capture the corrosion of degradable bone implants and to predict their residual strength, *Int. J. Mech. Sci.*, vol. 220, pp. 107143, 2022. DOI: [10.1016/j.ijmecsci.2022.107143](https://doi.org/10.1016/j.ijmecsci.2022.107143).
- [7] A. Gartzke, S. Julmi, C. Klose, A. Waselau, A. Meyer-Lindenberg, H.J. Maier, S. Besdo, and P. Wriggers, A simulation model for the degradation of magnesium-based bone implants, *J. Mech. Behav. Biomed. Mater.*, vol. 101, pp. 103411, 2020. DOI: [10.1016/j.jmbbm.2019.103411](https://doi.org/10.1016/j.jmbbm.2019.103411).
- [8] M. Barzegari, D. Mei, S.V. Lamaka, and L. Geris, Computational modeling of degradation process of biodegradable magnesium biomaterials, *Corros. Sci.*, vol. 190, pp. 109674, 2021. DOI: [10.1016/j.corsci.2021.109674](https://doi.org/10.1016/j.corsci.2021.109674).
- [9] S. Scheiner and C. Hellmich, Stable pitting corrosion of stainless steel as diffusion-controlled dissolution process with a sharp moving electrode boundary, *Corros. Sci.*, vol. 49, no. 2, pp. 319–346, 2007. DOI: [10.1016/j.corsci.2006.03.019](https://doi.org/10.1016/j.corsci.2006.03.019).
- [10] S. Scheiner and C. Hellmich, Finite volume model for diffusion- and activation-controlled pitting corrosion of stainless steel, *Comput. Methods Appl. Mech. Eng.*, vol. 198, no. 37–40, pp. 2898–2910, 2009. DOI: [10.1016/j.cma.2009.04.012](https://doi.org/10.1016/j.cma.2009.04.012).
- [11] O.C. Zienkiewicz and R.L. Taylor, *The Finite Element Method for Solid and Structural Mechanics*, Amsterdam, The Netherlands, Elsevier, 2005.
- [12] A. Torcasio, X. Zhang, H. Van Oosterwyck, J. Duyck, and G.H. van Lenthe, Use of micro-CT-based finite element analysis to accurately quantify peri-implant bone strains: a validation in rat tibiae, *Biomech. Model. Mechanobiol.*, vol. 11, no. 5, pp. 743–750, 2012. DOI: [10.1007/s10237-011-0347-6](https://doi.org/10.1007/s10237-011-0347-6).
- [13] R. Blanchard, A. Dejaco, E. Bongaers, and C. Hellmich, Intravoxel bone micromechanics for microCT-based finite element simulations, *J. Biomech.*, vol. 46, no. 15, pp. 2710–2721, 2013. DOI: [10.1016/j.jbiomech.2013.06.036](https://doi.org/10.1016/j.jbiomech.2013.06.036).
- [14] A. Ojdanic, E. Schafler, J. Horky, D. Orlov, and M. Zehetbauer, Strengthening of a biodegradable Mg–Zn–Ca alloy ZX50 after processing by HPT and heat treatment. In: *Magnesium Technology*, Springer, Cham, pp. 277–282, 2018.
- [15] H. Parkus, *Mechanik Der Festen Körper [Mechanics of Solids]*, 2 ed., Vienna, Austria, Springer-Verlag, 1966. [in German].
- [16] G.D. Muir and I.Q. Wishaw, Ground reaction forces in locomoting hemi-Parkinsonian rats: a definitive test for impairments and compensations, *Exp. Brain Res.*, vol. 126, no. 3, pp. 307–314, 1999. DOI: [10.1007/s002210050739](https://doi.org/10.1007/s002210050739).
- [17] T. Wehner, U. Wolfram, T. Henzler, F. Niemeyer, L. Claes, and U. Simon, Internal forces and moments in the femur of the rat during gait, *J. Biomech.*, vol. 43, no. 13, pp. 2473–2479, 2010. DOI: [10.1016/j.jbiomech.2010.05.028](https://doi.org/10.1016/j.jbiomech.2010.05.028).
- [18] F.P. Beer, E.R. Johnston, J.T. DeWolf, and D.F. Mazurek, *Statics and Mechanics of Materials*, vol. 1., McGraw-Hill, New York, 2011.
- [19] M.S. Qatu, In-plane vibration of slightly curved laminated composite beams, *J. Sound Vib.*, vol. 159, no. 2, pp. 327–338, 1992. DOI: [10.1016/0022-460X\(92\)90039-Z](https://doi.org/10.1016/0022-460X(92)90039-Z).
- [20] M.S. Qatu, Theories and analyses of thin and moderately thick laminated composite curved beams, *Int. J. Solids Struct.*, vol. 30, no. 20, pp. 2743–2756, 1993. DOI: [10.1016/0020-7683\(93\)90152-W](https://doi.org/10.1016/0020-7683(93)90152-W).
- [21] L. Dormieux, A. Molinari, and D. Kondo, Micromechanical approach to the behavior of poroelastic materials, *J. Mech. Phys. Solids.*, vol. 50, no. 10, pp. 2203–2231, 2002. DOI: [10.1016/S0022-5096\(02\)00008-X](https://doi.org/10.1016/S0022-5096(02)00008-X).
- [22] W. Kreher, Residual stresses and stored elastic energy of composites and polycrystals, *J. Mech. Phys. Solids.*, vol. 38, no. 1, pp. 115–128, 1990. DOI: [10.1016/0022-5096\(90\)90023-W](https://doi.org/10.1016/0022-5096(90)90023-W).
- [23] J. Barthélémy and L. Dormieux, A micromechanical approach to the strength criterion of Drucker-Prager materials reinforced by rigid inclusions, *Num. Anal. Meth. Geomech.*, vol. 28, no. 7–8, pp. 565–582, 2004. DOI: [10.1002/nag.368](https://doi.org/10.1002/nag.368).
- [24] A. Fritsch, L. Dormieux, C. Hellmich, and J. Sanahuja, Micromechanics of crystal interfaces in polycrystalline solid phases of porous media: fundamentals and application to strength of hydroxyapatite biomaterials, *J. Mater. Sci.*, vol. 42, no. 21, pp. 8824–8837, 2007. DOI: [10.1007/s10853-007-1859-4](https://doi.org/10.1007/s10853-007-1859-4).
- [25] H.W. Müllner, A. Fritsch, C. Kohlhauser, R. Reihnsner, C. Hellmich, D. Godlinski, A. Rota, R. Slesinski, and J. Eberhardsteiner, Acoustical and poromechanical characterisation of titanium scaffolds for biomedical applications, *Strain.*, vol. 44, no. 2, pp. 153–163, 2008. DOI: [10.1111/j.1475-1305.2007.00360.x](https://doi.org/10.1111/j.1475-1305.2007.00360.x).
- [26] K. Hofstetter, C. Hellmich, J. Eberhardsteiner, and H.A. Mang, Micromechanical estimates for elastic limit states in wood materials, revealing nanostructural failure mechanisms, *Mech. Adv. Mater. Struct.*, vol. 15, no. 6–7, pp. 474–484, 2008. DOI: [10.1080/15376490802142387](https://doi.org/10.1080/15376490802142387).
- [27] T.K. Bader, K. Hofstetter, C. Hellmich, and J. Eberhardsteiner, Poromechanical scale transitions of failure stresses in wood: from the lignin to the spruce level, *Z Angew. Math. Mech.*, vol. 90, no. 10–11, pp. 750–767, 2010. DOI: [10.1002/zamm.201000045](https://doi.org/10.1002/zamm.201000045).
- [28] B. Pichler and C. Hellmich, Upscaling quasi-brittle strength of cement paste and mortar: a multi-scale engineering mechanics model, *Cem. Concr. Res.*, vol. 41, no. 5, pp. 467–476, 2011. DOI: [10.1016/j.cemconres.2011.01.010](https://doi.org/10.1016/j.cemconres.2011.01.010).
- [29] B. Pichler, C. Hellmich, J. Eberhardsteiner, J. Wasserbauer, P. Termkhajornkit, R. Barbarulo, and G. Chanvillard, Effect of gel–space ratio and microstructure on strength of hydrating cementitious materials: an engineering micromechanics approach, *Cem. Concr. Res.*, vol. 45, pp. 55–68, 2013. DOI: [10.1016/j.cemconres.2012.10.019](https://doi.org/10.1016/j.cemconres.2012.10.019).
- [30] M. Königsberger, M. Hlobil, B. Delsaute, S. Staquet, C. Hellmich, and B. Pichler, Hydrate failure in ITZ governs concrete strength: a micro-to-macro validated engineering mechanics model, *Cem. Concr. Res.*, vol. 103, pp. 77–94, 2018. DOI: [10.1016/j.cemconres.2017.10.002](https://doi.org/10.1016/j.cemconres.2017.10.002).
- [31] J. Salençon, *Handbook of Continuum Mechanics: General Concepts Thermoelasticity*, Berlin, Germany, Springer Science & Business Media, 2001.
- [32] C.H. Turner, Skeletal adaptation to mechanical loading, *Clinic. Rev. Bone Miner. Metab.*, vol. 5, no. 4, pp. 181–194, 2007. DOI: [10.1007/s12018-008-9010-x](https://doi.org/10.1007/s12018-008-9010-x).
- [33] A.M. Parfitt, The physiological and clinical significance of bone histomorphometric data, R. Recker (Ed.), *Bone Histomorph. Tech. Interpret.*, Boca Raton, FL, USA, CRC Press Inc., pp. 143–223, 1983.
- [34] C. Morin, S. Avril, and C. Hellmich, Non-affine fiber kinematics in arterial mechanics: a continuum micromechanical investigation, *Z Angew. Math. Mech.*, vol. 98, no. 12, pp. 2101–2121, 2018. DOI: [10.1002/zamm.201700360](https://doi.org/10.1002/zamm.201700360).
- [35] C. Morin, C. Hellmich, Z. Nejm, and S. Avril, Fiber rearrangement and matrix compression in soft tissues: multiscale hypoeasticity and application to tendon, *Front. Bioeng. Biotechnol.*, vol. 9, pp. 725047, 2021. DOI: [10.3389/fbioe.2021.725047](https://doi.org/10.3389/fbioe.2021.725047).
- [36] H.C. Anderson, R. Garimella, and S.E. Tague, The role of matrix vesicles in growth plate development and biomineralization, *Front. Biosci.*, vol. 10, no. 1–3, pp. 822–837, 2005. DOI: [10.2741/1576](https://doi.org/10.2741/1576).

- [37] C. Morin and C. Hellmich, Mineralization-driven bone tissue evolution follows from fluid-to-solid phase transformations in closed thermodynamic systems, *J. Theor. Biol.*, vol. 335, pp. 185–197, 2013. DOI: [10.1016/j.jtbi.2013.06.018](https://doi.org/10.1016/j.jtbi.2013.06.018).
- [38] A.H. Ambre, D.R. Katti, and K.S. Katti, Biomaterialized hydroxyapatite nanoclay composite scaffolds with polycaprolactone for stem cell-based bone tissue engineering, *J. Biomed. Mater. Res.*, vol. 103, no. 6, pp. 2077–2101, 2015. DOI: [10.1002/jbm.a.35342](https://doi.org/10.1002/jbm.a.35342).
- [39] E. Macías-Sánchez, N.V. Tarakina, D. Ivanov, S. Blouin, A.M. Berzlanovich, and P. Fratzl, Spherulitic crystal growth drives mineral deposition patterns in collagen-based materials, *Adv. Funct. Mater.*, vol. 32, no. 31, pp. 2200504, 2022. DOI: [10.1002/adfm.202200504](https://doi.org/10.1002/adfm.202200504).
- [40] N. Reznikov, B. Hoac, D.J. Buss, W.N. Addison, N.M.T. Barros, and M.D. McKee, Biological stenciling of mineralization in the skeleton: local enzymatic removal of inhibitors in the extracellular matrix, *Bone.*, vol. 138, pp. 115447, 2020. DOI: [10.1016/j.bone.2020.115447](https://doi.org/10.1016/j.bone.2020.115447).
- [41] K.S. Probst and S. Lees, Visualization of crystal-matrix structure. In situ demineralization of mineralized turkey leg tendon and bone, *Calcif. Tissue Int.*, vol. 59, no. 6, pp. 474–479, 1996. DOI: [10.1007/s002239900160](https://doi.org/10.1007/s002239900160).
- [42] S. Lees, L.C. Bonar, and H.A. Mook, A study of dense mineralized tissue by neutron diffraction, *Int. J. Biol. Macromol.*, vol. 6, no. 6, pp. 321–326, 1984. DOI: [10.1016/0141-8130\(84\)90017-5](https://doi.org/10.1016/0141-8130(84)90017-5).
- [43] C. Hellmich and F.J. Ulm, Average hydroxyapatite concentration is uniform in the extracollagenous ultrastructure of mineralized tissues: evidence at the 1–10- μ m scale, *Biomech. Model. Mechanobiol.*, vol. 2, no. 1, pp. 21–36, 2003. DOI: [10.1007/s10237-002-0025-9](https://doi.org/10.1007/s10237-002-0025-9).
- [44] C. Hellmich and F.J. Ulm, Micromechanical model for ultrastructural stiffness of mineralized tissues, *J. Eng. Mech.*, vol. 128, no. 8, pp. 898–908, 2002. DOI: [10.1061/\(ASCE\)0733-9399\(2002\)128:8\(898\)](https://doi.org/10.1061/(ASCE)0733-9399(2002)128:8(898)).
- [45] C. Hellmich, J.F. Barthélémy, and L. Dormieux, Mineral–collagen interactions in elasticity of bone ultrastructure—a continuum micro-mechanics approach, *European J. Mech. A/Solids.*, vol. 23, no. 5, pp. 783–810, 2004. DOI: [10.1016/j.euromechsol.2004.05.004](https://doi.org/10.1016/j.euromechsol.2004.05.004).
- [46] L. Eberhardsteiner, C. Hellmich, and S. Scheiner, Layered water in crystal interfaces as source for bone viscoelasticity: arguments from a multiscale approach, *Comput. Meth. Biomech. Biomed. Eng.*, vol. 17, no. 1, pp. 48–63, 2014. DOI: [10.1080/10255842.2012.670227](https://doi.org/10.1080/10255842.2012.670227).
- [47] A. Fritsch, C. Hellmich, and L. Dormieux, Ductile sliding between mineral crystals followed by rupture of collagen cross-links: experimentally supported micromechanical explanation of bone strength, *J. Theor. Biol.*, vol. 260, no. 2, pp. 230–252, 2009. DOI: [10.1016/j.jtbi.2009.05.021](https://doi.org/10.1016/j.jtbi.2009.05.021).
- [48] V. Kumbolder, C. Morin, S. Scheiner, and C. Hellmich, Hierarchical elastoplasticity of cortical bone: observations, mathematical modeling, validation, *Mech. Mater.*, vol. 198, pp. 105140, 2024. DOI: [10.1016/j.mechmat.2024.105140](https://doi.org/10.1016/j.mechmat.2024.105140).
- [49] M. Touratier, An efficient standard plate theory, *Int. J. Eng. Sci.*, vol. 29, no. 8, pp. 901–916, 1991. DOI: [10.1016/0020-7225\(91\)90165-Y](https://doi.org/10.1016/0020-7225(91)90165-Y).
- [50] P. Kuttke, A. Kurfürst, S. Scheiner, and C. Hellmich, Sequential 1D/2D finite element analyses of tramway rails under bending and restrained torsion, based on the principle of virtual power, *Mech. Adv. Mater. Struct.*, vol. 28, no. 11, pp. 1147–1169, 2021. DOI: [10.1080/15376494.2019.1647317](https://doi.org/10.1080/15376494.2019.1647317).
- [51] E. Carrera, M. Filippi, and E. Zappino, Free vibration analysis of rotating composite blades via Carrera unified formulation, *Compos. Struct.*, vol. 106, pp. 317–325, 2013. DOI: [10.1016/j.compstruct.2013.05.055](https://doi.org/10.1016/j.compstruct.2013.05.055).
- [52] A. Pagani and E. Carrera, Large-deflection and post-buckling analyses of laminated composite beams by Carrera unified formulation, *Compos. Struct.*, vol. 170, pp. 40–52, 2017. DOI: [10.1016/j.compstruct.2017.03.008](https://doi.org/10.1016/j.compstruct.2017.03.008).
- [53] P. Germain, The method of virtual power in continuum mechanics. part 2: microstructure, *SIAM J. Appl. Math.*, vol. 25, no. 3, pp. 556–575, 1973. DOI: [10.1137/0125053](https://doi.org/10.1137/0125053).
- [54] R. Höller, M. Aminbaghai, L. Eberhardsteiner, J. Eberhardsteiner, R. Blab, B. Pichler, and C. Hellmich, Rigorous amendment of Vlasov’s theory for thin elastic plates on elastic Winkler foundations, based on the principle of virtual power, *European J. Mech. A/Solids.*, vol. 73, pp. 449–482, 2019. DOI: [10.1016/j.euromechsol.2018.07.013](https://doi.org/10.1016/j.euromechsol.2018.07.013).
- [55] R. Scharf, B. Pichler, R. Heissenberger, B. Moritz, and C. Hellmich, Data-driven analytical mechanics of aging viscoelastic shotcrete tunnel shells, *Acta Mech.*, vol. 233, no. 8, pp. 2989–3019, 2022. DOI: [10.1007/s00707-022-03235-1](https://doi.org/10.1007/s00707-022-03235-1).
- [56] D. Capecchi, History of Virtual Work Laws: A History of Mechanics Prospective, Volume 42, Milan, Italy, Springer Science & Business Media, 2012.
- [57] F. dell’Isola and A. Misra, Principle of virtual work as foundational framework for metamaterial discovery and rational design, *Comptes Rendus Mécanique.*, vol. 351, no. S3, pp. 65–89, 2023. DOI: [10.5802/crmeca.151](https://doi.org/10.5802/crmeca.151).

Appendix. Bending beam equilibrium derived from principle of virtual power

So as to motivate the equilibrium conditions of Eq. (3), we here resort to the principle of virtual power (PVP) [49, 53–55], one of most versatile fundamentals of mechanics with roots going back to ancient times [56, 57]. The PVP provides a firm anchorage of beam theory in the 3D continuum mechanics framework. Accordingly, we adopt an arbitrary virtual rigid body rotational motion of a rigid cross section around the y - and z -axes,

$$\hat{\mathbf{v}}(x, y, z) = \hat{\omega}_y(x)z\mathbf{e}_x - \hat{\omega}_z(x)y\mathbf{e}_x \quad \forall \hat{\omega}_y(x), \hat{\omega}_z(x) \in \mathbb{R} \quad (\text{A1})$$

with $\hat{\omega}_y$ and $\hat{\omega}_z$ being the components of virtual angular velocity vector $\hat{\boldsymbol{\omega}} = \hat{\omega}_y\mathbf{e}_y + \hat{\omega}_z\mathbf{e}_z$. When considering a situation where this virtual velocity field does not produce any power of external forces, then the virtual power of the internal forces need to vanish in an equilibrated 3D classical continuum. This reads mathematically as

$$\mathcal{P}^{int} = - \int_V \boldsymbol{\sigma} : \nabla^S \hat{\mathbf{v}} dV = 0 \quad (\text{A2})$$

with ∇^S standing for the symmetrized nabla (or gradient) operator. Insertion of (A1) into (A2) yields

$$\begin{aligned} & \int_{-l/2}^{l/2} \int_A \sigma_{xx} z dA \frac{d\hat{\omega}_y}{dx} dx + \int_{-l/2}^{l/2} \int_A \sigma_{xz} dA \hat{\omega}_y dx \\ & - \int_{-l/2}^{l/2} \int_A \sigma_{xx} y dA \frac{d\hat{\omega}_z}{dx} dx - \int_{-l/2}^{l/2} \int_A \sigma_{xy} dA \hat{\omega}_z dx = 0 \end{aligned} \quad (\text{A3})$$

$\forall \hat{\omega}_y(x), \hat{\omega}_z(x) \in \mathbb{R}$

The quantities performing power on angular velocities and their gradients are called shear forces and bending moments, respectively; this yields

$$M_y = \int_A \sigma_{xx} z dA \quad M_z = - \int_A \sigma_{xy} dA \quad (\text{A4})$$

$$S_y = \int_A \sigma_{xy} dA \quad S_z = \int_A \sigma_{xz} dA \quad (\text{A5})$$

and insertion of (A4) and (A5) into (A3) yields, after integration by parts, that

$$\begin{aligned} & M_y \hat{\omega}_y|_{-l/2}^{l/2} - \int_{-l/2}^{l/2} \left(\frac{dM_y}{dx} - S_z \right) \hat{\omega}_y dx \\ & + M_z \hat{\omega}_z|_{-l/2}^{l/2} - \int_{-l/2}^{l/2} \left(\frac{dM_z}{dx} + S_y \right) \hat{\omega}_z dx = 0 \end{aligned} \quad (\text{A6})$$

$\forall \hat{\omega}_y(x), \hat{\omega}_z(x) \in \mathbb{R}$

This readily yields the equilibrium conditions (3).